version on March 19, 1998

SUMER MEASUREMENTS OF NON-THERMAL MOTIONS: CONSTRAINTS ON CORONAL HEATING MECHANISMS

Jongchul Chae
Big Bear Solar Observatory, New Jersey Institute of Technology
40386 North Shore Lane, Big Bear City, CA 92314-9672
chae@bbso.njit.edu

and

Udo Schühle
Max-Planck-Institut für Aeronomie, D-37191 Katlenburg-Lindau, Germany
schuehle@linmpi.mpg.de

and

Philippe Lemaire
Institut d'Astrophysique Spatiale, Unité Mixte CNRS-Universite, Paris XI bât.121, F-91405 Orsay, France
lemaire@iaslab.ias.fr

ABSTRACT

We have determined non-thermal velocities in the quiet Sun at temperatures between 10^4 K and 2×10^6 K by measuring widths of a number of EUV and FUV lines taken with SUMER on board the SOHO spacecraft. The broadenings due to the SUMER instrument and the finite opacity in each line have been carefully examined. The non-thermal velocity at temperatures below 2×10^4 K is smaller than 10 km s^{-1}. The velocity increases with temperature, reaches a peak value of 30 km s^{-1} around 3×10^5 K, and then decreases with temperature. The coronal non-thermal velocity is about 20 km s^{-1}. There exists a strong correlation between intensity and non-thermal velocity at temperatures $2 \times 10^4 - 1 \times 10^5$ K. The correlation at higher temperatures weakens as temperature increases. Furthermore, there is a spatial correlation between the non-thermal velocities inferred from a set of any two lines with temperatures below 2×10^5 K. Neither significant center-to-limb variation nor meaningful dependence on the integration time was found from the measured non-thermal velocities. We have discovered the existence of high velocity components in the observed S VI λ933.4 line profiles. The average non-thermal velocity and intensity fraction of this S VI line high velocity component are found to be 55 km s^{-1} and 0.25, respectively.

Observational characteristics of non-thermal motions carry some problems which should be solved in interpreting observed non-thermal motions in terms of either unresolved loop flows or Alfvén waves. The isotropic and very small-scale nature of the observed non-thermal motions appears to be suited for the MHD turbulence interpretation of non-thermal motions. The turbulent heating rates inferred from the measured non-thermal motions can account for the radiative loss throughout the transition region and corona if the non-thermal motions are truly turbulent motions whose mechanical energy is injected at a scale of 1000 km (Kolmogorov type turbulence) or 15 km (Kraichnan type turbulence). The existence of high velocity components at temperatures $6 \times 10^4 - 2 \times 10^5$ K appears as observational evidence supporting nanoflare heating at these temperatures.

Subject headings: Sun: UV radiation — Sun: transition region — Sun: Corona — MHD — turbulence

1. INTRODUCTION

It is now widely believed that coronal heating is of magnetic origin and the upper atmosphere is excited by interactions between the magnetic field and mass motion in the photosphere. Various physical processes have been considered as possible mechanisms for photospheric driving and coronal dissipation including MHD waves (Ionson 1982; Hollweg 1984; Poedts, Goossens & Kerner 1990; Ofman, Davila & Steinolfson 1995), nanoflares (Parker 1983a, 1983b, 1988), and MHD turbulence (Gómez & Ferro Fontán 1988, 1992; Heyvaerts & Priest 1992; Inverarity, Priest & Heyvaerts 1995; Inverarity & Priest 1995a, 1995b). Recent reviews of these mechanisms have been provided by Zirker (1993) and references therein. A proper evaluation of each mechanism requires observations of motions at the photospheric footpoints as well as much improved measurements of velocity fluctuations in the transition region and corona as noted by Zirker (1993).

The purpose of this work is to seek observational evidence to decide on a specific coronal heating mechanism, based upon measurements of non-thermal motions in the upper atmosphere. Previous EUV and FUV measurements (Boland et al. 1975; Doschek et al. 1976; Mariska et al. 1978; Bruner & McWhirter 1979; Dere et al. 1987; Hassler et al. 1990; Dere & Mason 1993; Doyle et al. 1997) have revealed that most solar EUV and FUV lines are broader than those expected from thermal broadening, which is usually regarded as a manifestation of unresolved mass motions (non-thermal motions) of the plasma with temperatures in the range $2 \times 10^4 - 10^6$ K. The measured non-thermal velocities range from 5 km s^{-1} to 30 km s^{-1}. In the previous experiments, however, the temperature dependence of non-thermal velocities has not been well established especially because of the scarcity of measurements of lines formed in the upper transition region and corona. There has been also a controversy on how the non-thermal broadening is correlated with the line intensity and Doppler shift (e.g., Athay et al. 1983; Dere et al. 1984).

The nature of the observed non-thermal motions is not yet clear. They could be fine scale laminar flows, waves, or turbulence, each of which may play a role in energy transport and heating in the corona. Since it is believed that the mechanical energy required for coronal heating is transported from the lower atmosphere (low temperatures) to the upper atmosphere (high temperatures), looking into the temperature dependence of non-thermal motions in the transition region and corona will be helpful in clarifying the dominant coronal heating mechanism as well as the physical nature of non-thermal motions.

The SUMER instrument on board the SOHO spacecraft provides us with unprecedented opportunity for studying non-thermal motions. First, it can observe a number of EUV and FUV lines covering plasma temperatures between 10^4 K and 2×10^6 K. It is noted that the lines having formation temperatures above 3×10^5 K such as the O VI, Ne VIII, Mg X and Fe XII lines have been rarely measured in the past experiments. Second, it has the capability of measuring bulk and random motions with a good accuracy of 1-2 km s^{-1} at a spatial resolution of $1'' \times 2''$. Finally, its capability of an uninterrupted long run of quiet Sun observations in the solar minimum period provides a rare opportunity for obtaining a good number of quiet Sun samples for studies of non-thermal motions. Recently Seely et al. (1997) measured the widths of the coronal lines outside the limb using SUMER to determine non-thermal motions and ion temperatures in the corona. The present study will deal with the observations made mostly near disk center and will measure a number of lines covering both the transition region and corona.

2. OBSERVATION AND DATA REDUCTION

Our EUV and FUV spectral data have been taken from SUMER observations performed during the period from April 1996 to April 1997. Good descriptions of the characteristics and performance of the SUMER instrument are found in Wilhelm et al. (1995, 1997) and Lemaire et al. (1997). We have selected our data to meet the following criteria. We confined our study to quiet Sun observations, taking full advantage of the solar minimum period. Most of them were made at disk center, but a few observations made near the limb were also included to examine any center-to-limb dependence. We used only those lines which are strong enough to have good signal-to-noise ratios and are well separated from neighboring lines. Different integration times were chosen depending on the strength of the measured lines. For example, stronger lines such as the O VI λ1037.6 line were integrated for 20 s and weaker lines such as the C IV λ1548.2 line, which appears weak because of the low sensitivity at longer wavelengths, for 300 s. The measured lines cover temperatures between 10^4 K and 2×10^6 K. Figure 1 illustrates a few among the lines selected for measurements of non-thermal motions. The presented lines were taken from the same slit image of a quiet region so that they have exactly the same observing time and pointing.

SUMER spectral data usually need to be corrected for the detector sensitivity pattern (flatfield correction) and geometric distortion prior to analysis. Corrections of the detector sensitivity pattern are made by dividing the observed spectral data by the flat image taken closest in time to the observation. The uncertainty in the flatfield correction arising from the time variation of the detector pattern can produce noise proportional to the signal (Chae, Yun & Poland 1998), causing random errors in measuring the line parameters, but we expect its effect on spatially averaged line widths is negligible. Next, we consider the effect of geometric distortion of the detectors. The distortion should be carefully corrected when measuring the spectral and spatial positions of line emission. Its effect on the line width is less severe than that on the line position because the distortion effect on the line width is of a second order. For this reason we have not applied the geometric distortion correction in the present study. Not applying this kind of correction is especially important when measuring the widths of narrower lines, since the interpolation required for geometric distortion correction may cause significant additional broadening.

We have measured the line width at every spatial element of size $1'' \times 1''$ in a given field of view by applying non-linear Gaussian fitting to the observed line profiles, the detail of which method was described by Chae, Yun & Poland (1998). Lines well separated from other lines are fitted by a single Gaussian, but lines blended by the neighboring lines are fitted by two or three Gaussians to minimize the blending effect on the line width measurements. A best fit is determined by taking into account the noise characteristics of SUMER data and produces the Gaussian width σ_x of a line, which is defined in a Gaussian line profile

$$I_x = \sum_x I_p \exp\left(-\frac{1}{2}\left(\frac{x - x_c}{\sigma_x}\right)^2\right) \tag{1}$$

where x is the value of the detector pixel in the spectral direction. To increase the signal to noise ratio in the data, a spectral profile at each spatial element was usually smoothed over 3 neighboring pixels along the slit direction, which corresponds to $3''$ along the slit. Thus the practical spatial resolution of the results we present in this paper is reduced to about $1'' \times 3''$ which is a little larger than the pixel resolution of

$1'' \times 1''$ and the SUMER spatial resolution of $1'' \times 2''$ usually achieved in non-smoothed data (Lemaire et al. 1997). We found no systematic difference between the spatial averages of line widths measured from the raw spectral profiles and those from the spectral profiles smoothed in the above way, but the smoothed profiles yield less spatial fluctuations in line widths because of the higher signal to noise ratios. This kind of smoothing was particularly useful in reducing the noise introduced by the uncertainty in the flat field correction without degrading the spectral resolution. Hence we neglected this kind of noise in the smoothed spectral profiles and considered only the photon noise in the fitting process.

3. RESULTS

The measured line widths consist of two components: instrumental broadening and solar broadening. If both the instrumental and solar profiles are Gaussian, the measured Gaussian width, σ_x is given by

$$\sigma_x^2 = \sigma_{x,instr}^2 + \sigma_{x,solar}^2. \tag{2}$$

The full width at half maximum (FWHM) of the instrumental profile is equal to $2\sqrt{2\ln 2}\sigma_{x,instr}$. Sometimes it is more convenient to work with velocities than pixels or wavelengths, so we introduce the velocities

$$v_{meas} \equiv \sqrt{2}\sigma_x \frac{d\lambda}{dx}\frac{c}{\lambda}; \;\; v_{inst} \equiv \sqrt{2}\sigma_{x,instr}\frac{d\lambda}{dx}\frac{c}{\lambda}; \;\; v_{solar} \equiv \sqrt{2}\sigma_{x,solar}\frac{d\lambda}{dx}\frac{c}{\lambda} \tag{3}$$

as measures of the different kinds of line width. The dispersion $d\lambda/dx$ has a value ranging from 44.7 to 41.8 mÅ/pixel at first order wavelengths 800-1600 Å. For an optically thin line, the solar broadening v_{solar} is given by

$$v_{solar} = \sqrt{\frac{2kT}{M} + \xi^2} \tag{4}$$

where M is the mass of the atom emitting the line, ξ is the most probable speed of the non-thermal motion, and T is the temperature of the atom, which is assumed to be equal to the electron temperature. In the case of optically thick lines, opacity also affects the line widths so that the above relation does not hold. We will evaluate the opacity effect in each line later in this section.

Following a conventional approach (e.g., Dere & Mason 1993), the formation temperature of each line has been determined by maximizing the contribution functions $(n_i/n_{el})T^{-1/2}\exp(-E/kT)$ where E is the energy of the upper level measured from the ground level and n_i/n_{el} is the relative ion abundance taken from Arnaud & Rothenflug (1985). The line formation temperatures determined in this way are listed in Tables 1, 2 and 4. Most of contribution functions have a single well-defined peak except the S I lines. The S I lines display three peaks around $\log T = 3.75$, 4.05, and 4.35 depending sensitively on the excitation energy. In view of the crudeness of the method, this excessive sensitivity and the peaks occurring at the lower and higher temperatures may be not real. A more conservative choice would be to stay on the middle peak, which yields nearly the same formation temperatures for all the S I lines. This is the reason why the S I 1300.9 line formation temperature is much different from Dere & Mason's (1993) value.

3.1. Instrumental Broadening

The proper determination of instrumental width is important in accurately determining the solar broadening of each line. We examine the SUMER instrumental broadening employing two different approaches: 1) using laboratory measurements of platinum (Pt) lines and 2) using in-flight measurements of the narrowest neutral lines.

The first method is relatively simple. Using the Gaussian fitting described earlier, we measured the line widths of several platinum (Pt) lines which were emitted by a hollow cathode source and recorded with the A detector in the laboratory before launch. The measured widths do not show any significant dependence on the line wavelength and have a FWHM value of about 1.95 pixels. Since the intrinsic broadening of the laboratory Pt lines should be very small compared with the measured line widths, the measured Pt line width must be mostly due to instrumental broadening. This value is close to the theoretical value of about 2 pixels computed from the ray tracing with the grating and other optical elements taken into account. The in-flight spectrometer focusing adjustment tries to keep the spectrometer performances at the measured laboratory values. But there is still a possibility that in-flight instrumental broadening will deviate from laboratory instrumental broadening. Therefore it is necessary to examine the instrumental broadening based on the in-flight data.

The second method can be used to examine the in-flight instrumental broadening. It is obvious that the instrumental width should be less than observed line widths. Therefore the narrowest observed line width will give us an upper bound of the instrumental broadening. We have measured the width of the O I λ1355.6 line at every point in a quiet region observed on 3 August 1996 near the disk center. The average value of v_{meas} in this region is found to be 15.4 km s^{-1}, and some spatial points display smaller values down to 13.7 km s^{-1}. Figure 2 shows the integrated intensity and width maps of a sub-region surrounding such a point, and the line profile at the point together with the result of two Gaussian fitting. Both the spatial width map and the fit result support the small line width of 13.7 km s^{-1} at point A is not due to an error, but real. Consequently, v_{inst} should be less than 13.7 km s^{-1}. Assuming that $\xi = 0$ km s^{-1} at point A and subtracting the thermal contribution of 4.0 km s^{-1}, we obtain a v_{inst} estimate of 13.1 km s^{-1}, which corresponds to a FWHM instrumental width of 2.3 detector pixels. This value is slightly greater than 2.0 detector pixels, the value found by Wilhelm et al. (1997) from a simple FWHM estimate of the S I λ1300.9 line width. The difference may be partly attributed to the different measurement scheme. Since we are using Gaussian fitting, the lower intensity wing part may also contribute to line width measurements, resulting in a slightly larger value than the width value estimated from the half maximum intensity values only.

We have measured the widths of many narrow neutral lines from observations made from 3 through 5 August 1996 and determined their solar broadenings after correcting for the instrumental width of 2.3 pixels. The results are listed in Table 1. Each width value presented in the table is an average over all the points in a region having the specified field of view (FOV). It should be noted that the two measurements of the O I λ1355.6 line on the different days, August 3 and 5, produced about the same solar broadening of 8.0 km s^{-1}. This indicates that the instrumental broadening practically did not change during these days. Even though this value of solar broadening is a little larger than 6.0 km s^{-1} found from Skylab (Kjeldseth-Moe & Nicolas 1977; Mariska, Feldman & Doschek 1978) and HRTS (Dere & Mason 1993) experiments, the difference may not be significant. In the S I λ1300.9 line, our estimate agrees quite well with the value of 6.2 km s^{-1} obtained by Dere & Mason (1993). Therefore we see that our estimate of the instrumental width is reasonable and may allow us to compare our measurements of non-thermal velocities with the previous measurements with a consistency.

At this point, we feel it necessary to deal with the probable error arising from undersampling by the detector. Since the observed FWHMs of these lines are on the order of 2-3 detector pixels, it would seem that measurements of these lines could vary by significant amounts depending on how the line fell on the detector pixels. We see, however, that this is not the case. It is recalled that the O I λ1355.5 line widths measured on different days give about the same value and that the measured widths of the three C I lines 1244.5, 1249.4, 1252.2 listed in Table 1 are about the same within an accuracy of 1 km s^{-1}. These good agreements are strong evidence that even the widths of narrow neutral lines can be measured quite accurately. This is possible mainly because we have employed the non-linear Gaussian fitting in measuring the line width. Usually the profile of a single narrow line is covered by about 10 pixels (See Figure 2) and these are enough to constrain the three line parameters of peak, position and width accurately enough if the signal-to-noise ratio is high enough and the line profile does not deviate much from a Gaussian function. On the other hand, the accuracy of the moment method, which is a kind of integration scheme, may be limited by the pixel size and the number of data points as well as the signal to noise ratio of the data.

The time variation of the SUMER spectrograph instrumental width during the period of 1996 and 1997 has been examined by measuring the widths of the narrow neutral lines listed in Table 1 on different days. If we assume the solar broadenings of these narrow lines do not vary in the quiet Sun, it is trivial to determine the instrumental widths from the measured widths. We have found that when the A detector is used, the temporal fluctuation of the instrumental width is about 0.15 pixels, and the mean value is 2.35 pixels. The mean value is close to the value 2.3 pixels we determined from the O I λ1355.5 line observations made on August 3. It is likely that the true temporal fluctuation of the instrumental width may be less than 0.15 pixels since a part of the observed line width fluctuations may be attributed to the possible variation of solar broadenings over observing regions. In the case of detector B observations, it has been found that the average instrumental width value is about 3.0 pixels and its fluctuation is about 0.5 pixels. Both values are significantly larger than the corresponding values of detector A observations. The spectral resolution of the spectrometer with the B detector appears degraded mainly because of the residual aberrations arising from the off-axis grating diffraction angle. It can be also affected by the spread function of the detector which depends on the gain of the microchannel plate when the applied voltage does not provide gain saturation. To increase the lifetime of the detector, the microchannel plate gain is usually allowed to decrease slowly with time once it is set at the limit of gain saturation. During this gain drift, the location of the cloud of electrons generated by an incident photon is less accurate, resulting in a broader line profile.

3.2. Opacity Effect

If a line is not optically thin, it is broadened also by opacity, which may lead to an overestimation of its non-thermal motion. It has been shown that the Si III λ1206 line has non-negligible opacity even in disk observations (Feldman, Doschek, & Patterson 1976). The strong C II λ1334.5 and 1335.7 lines also often show evidence of opacity (Dere & Mason 1993). On the other hand, Dere & Mason (1993) have shown that opacity is not significant in the C IV λ1548.2 and 1550.8 lines. Thus it appears that the opacity effect is significant especially in the lines formed at lower temperatures.

Table 2 presents v_{meas} and v_{solar} of more EUV and FUV lines formed at lower temperatures in addition to the lines given in Table 1. All of the observations presented in the tables were made with the use of the A detector which gives a better spectral resolution. We see from Tables 1 and 2 that the three neutral lines C I λ1315.9, N I λ1319.7 and O I λ1355.6 have much smaller line widths than other neutral lines emitted by the same atoms. For example, we find that the O I λ 1355.5 line has a much smaller v_{solar} of 8.0 km s^{-1} than the other O I line λ1040.9, which has a v_{solar} of 14.5 km s^{-1}. The most plausible explanation for the width difference between the O I λ1355.6 and 1040.9 lines seems to be opacity.

Whether a line is optically thin or not can be tested based on the intensity ratio of two lines in a multiplet (See, for example, Zirin 1988). Dere & Mason (1993) applied this method to the C IV λ1548 line and found that its opacity in disk observations is less than 0.6 and has little effect on the line width. Following Dere & Mason (1993), we presented the theoretical intensity ratio r of O I λ1040.9 to 1041.7 line,

$$r = \frac{\int 1 - \exp[-\tau_0 \exp(-(v/v_{solar})^2)]dv}{\int 1 - \exp[-\tau_0/\alpha \exp(-(v/v_{solar})^2)]dv} \tag{5}$$

as a function of the optical depth τ_0 at the center of O I λ1040.9 line in Figure 3. Here α is the opacity ratio, which is equal to 3 in these lines. In the optically thin limit, the intensity ratio is reduced to α. The observed average intensity ratio, however, is found to be 1.14 with a standard deviation of 0.07, which indicates the O I λ1040.9 line has an optical depth greater than 10. The same method has been applied also to the pair of O I $\lambda\lambda$1355.6/1358.5 lines and it is found that the line O I λ1355.6 line has an opacity of 0.5. This proves that the width difference between the O I λ1355.6 and 1040.9 lines is due to opacity. The same argument can be applied also to the width differences found in the C I and N I lines. As a result, we find that among the neutral lines only the narrower lines C I λ1315.9, N I λ1319.7 and O I λ1355.6 are optically thin and can serve as good diagnostics of non-thermal motions in the chromosphere and low transition region.

Table 3 presents the opacities of a number of lines estimated from the observed disk center line ratios. It is noticeable that the S II lines formed at the lower transition region are optically thin. The C II λ 1036.3 and 1037.3 lines have significant opacities. Even though we have not estimated the opacities of the lines emitted by the singly ionized atoms Fe II, N II and Si II, they seem to be all optically thick because they have larger line widths than the optically thin lines formed at the same temperatures. All the resonance lines of the ions Si IV, C IV, N V, S VI and O VI formed at the middle transition region as well as the coronal Mg X resonance lines are optically thin in disk observations.

The C II lines are important in determining the non-thermal velocity at temperatures around $3-4\times10^4$ K. But these lines have significant opacities so that Equation 4 can not be used to determine non-thermal velocity ξ since the solar broadening v_{solar} is larger than $\sqrt{2kT/M+\xi^2}$. Nevertheless, if opacity is not very large, even an optically thick line profile is still close to a Gaussian so that the profile can be fitted by a Gaussian to yield the solar broadening v_{solar}. Figure 4 shows the theoretically calculated ratios of v_{solar} to $\sqrt{2kT/M+\xi^2}$ as functions of opacity in the three different cases of $\sqrt{2kT/M+\xi^2}/v_{ins}$. We find from the figure that the v_{solar} of the line C II λ1036.3 having an opacity of about 3 is 1.2 times $\sqrt{2kT/M+\xi^2}$, which allows us to determine ξ from v_{solar}.

3.3. Temperature Dependence

Among the lines given in Tables 1 and 2, we carefully selected only those lines which can best represent the non-thermal motion at each temperature. All the neutral lines except the three narrow lines C I λ1315.9, N I λ1319.7 and O I λ1355.6 are excluded because they appear to be optically thick. For the same reason, the Fe II, N II and Si II lines are also excluded except the optically thin S II λ1253.8 line. Even though the C II lines have significant opacities, they are included because of their importance in the determination of temperature dependence around 3.5×10^4 K. These lines have been corrected for opacity. We include all the optically thin resonance lines of the ions Si IV, C IV, N V, S VI, O VI and Mg X except the lines highly affected by blending due to other lines. A caution should be drawn to the O VI λ1031.9 line because it seems to be affected by the unresolved Fe III λ1032.1 line and produces a little larger line widths than the other resonance line O VI λ1037.6. The forbidden line O IV λ1401.1 appears inadequate for the study of non-thermal motions because of its weakness. As pointed out by Dere & Mason (1993), the weak wing of this line can not contribute to the measured width due to the relative high continuum level so that its non-thermal velocity always tends to be underestimated.

Figure 5 shows the relation of ξ versus temperature in the quiet Sun disk observations. Each data point in the plot represents the spatially averaged value in each day's observation. The non-thermal velocities of different lines display a clear temperature dependence. The non-thermal motion speed ξ increases with temperature, reaches its peak around 3×10^5 K, and then decreases at higher temperatures.

Table 4 summarizes our results, which presents the spatial average and root-mean-square(RMS) fluctuation of non-thermal velocity in each line. The lines formed in the upper transition region and corona have a tendency to produce different spatial averages on different days. The amount of the day-to-day variation is usually of the same order as the RMS fluctuation estimated from one day observation. The day-to-day variations of the spatial average in these lines seem to arise from our small field of view which may not properly represent the quiet Sun at least in high temperature lines. Thus in every line where more than one day of observations is available, we took the ensemble average of the spatial averages obtained on different days to get a better quiet Sun representative value.

The O I λ1355.6 line has a non-thermal motion of 7 km s^{-1} which is greater than the 4 km s^{-1} estimated from Skylab(Doschek et al. 1976; Kjeldseth-Moe & Nicolas 1977) and HRTS (Dere & Mason 1993) experiments. The N I λ1319.7 line has a non-thermal velocity of 6.7 km s^{-1}, which is very close to that of the O I line. This appears physically reasonable because these lines have about the same formation temperature. The C I λ1315.9 line which is formed at a lower temperature than the above two lines has a smaller value of 3.7 km s^{-1}. The S II λ1253.8 line has ξ = 14.6 km s^{-1}, which is much smaller than the limb value of 22 km s^{-1} obtained by Kjeldseth-Moe & Nicolas (1977). It is suspected that this line becomes optically thick at the limb.

The Si IV lines and the C IV lines have been most frequently measured in previous experiments. We obtained the non-thermal motions of the Si IV λ1393.8, 1402.8 lines which are nearly the same as the values reported by Doschek et al.(1976), Doschek, Mariska & Feldman (1981) and Dere & Mason (1993). As expected, the two C IV resonance lines produce the same value of non-thermal motion of 25 km s^{-1}, which is equal to the average of the two line widths obtained by Doschek, Mariska & Feldman (1981) and slightly smaller than the value of 28 km s^{-1} measured by Dere & Mason(1993). Dere & Mason (1993) attributed their large value of the C IV line non-thermal motion to extended wings of the line profiles which show emission mostly in excess of their central Gaussian portions. Our C IV data are not so good as to be used for this kind of examination because the detector sensitivity is low in the wavelength regime around the C IV lines. Instead we will use the S VI λ933.4 line to examine the emission in the wing later in this section. Our N V non-thermal velocities are nearly the same as the values obtained by Doschek et al. (1976). On the other hand, the HRTS experiment (Dere & Mason 1993) gives significantly lower values of 16-17 km s^{-1}. It seems that this difference is mainly due to the low sensitivity of these lines in the HRTS experiments which can not reveal fully the wings. The S VI lines have never been measured in the previous experiments. We find that the S VI λ933.4 line has a non-thermal velocity of 28 km s^{-1} , which is comparable to the values of the N V ions having about the same formation temperature. The O VI λ1037.6 line having a higher formation temperature has the peak non-thermal velocity of about 29 km s^{-1}.

Our measurements of the upper transition region line Ne VIII λ770.4 and the coronal lines Mg X λ625.0 and Fe XII λ 1242.0 show that the non-thermal velocity decreases with temperature above 3×10^5

K. The Ne VIII λ770.4 line is a good diagnostic of non-thermal motions in the upper transition region, which yields a non-thermal velocity of 25 km s^{-1}. The non-thermal velocity of the coronal Mg X λ625 line measured near disk center is 23 km s^{-1}, which is a little smaller than, but not much different from the disk value of 26 km s^{-1} obtained by Hassler et al. (1990). It is also interesting to note that our value is very close to the non-thermal velocity of 22 km s^{-1} at 30$''$ above the limb measured by Seely et al. (1997). As far as we know, the width of the forbidden line Fe XII λ1242.0 has never been measured from quiet Sun disk observations because the line is too weak. For the first time, we measured this line from quiet Sun disk observations and obtained the non-thermal velocity of 16 km s^{-1} which is slightly smaller than the limb value of 18 km s^{-1} determined by Cheng, Doschek & Feldman (1979). In view of the large probable error in determining the line width from disk observations, the agreement seems quite good.

3.4. Spatial Distributions

The standard deviation of the non-thermal velocity in each line, σ_ξ in Table 4, is contributed not only by the random errors in the measurements, but also by the intrinsic spatial fluctuation of the non-thermal motion, particularly in the case of the strong lines like the C II, Si IV, N V, S VI, O VI and Ne VIII lines. As seen from Figure 6, the spatial distributions of non-thermal velocities of the C II and O VI lines are far from being random. Roughly speaking the non-thermal velocities are larger in bright network than in dark cell interior. It is this cell-network contrast that is mainly responsible for σ_ξ and the spatial correlations between intensity and non-thermal motion of these lines presented in Figure 7. As can be seen from Figures 6 and 7, the C II line which are formed below 10^5 K has a strong correlation between intensity and non-thermal velocity. But, the correlation is less strong in the O VI line which is formed at a temperature above 10^5 K. It appears that the strongest correlation is found in the Si IV and C IV lines (see Figure 8) and the correlation decreases with temperature above 10^5 K. The correlation becomes very weak in the upper transition region and corona represented by the Ne VIII and Mg X lines. The computed correlation coefficients listed in Table 4 summarize these results.

The spatial correlation between two lines with different formation temperatures will give us additional information which is helpful for understanding the physical nature of non-thermal motions and the structure of the transition region. As can be seen from Figure 9, there is a correlation between the N V line formed in the middle transition region and the S II line formed in the lower transition region. A similar correlation exists also in the pair of the C II and O VI lines, but is weaker than the pair of the S II and N V lines. The correlation becomes much weaker in the pair of the C IV and Ne VIII lines and in the pair of the N V and Mg X lines.

Our results confirm the findings of Dere et al. (1984) and Dere & Mason (1993) that the intensity and non-thermal velocity are positively correlated in the Si IV and C IV lines. They also suggest that 1) the lower and middle transition region characterized by the temperatures of $2 \times 10^4 - 2 \times 10^5$ K may consist of coherent structures and 2) the structure of the upper transition region and corona with temperatures high above 2×10^5 K may be much different from that of the cooler transition region.

3.5. High Velocity Components

It was first recognized by Kjeldseth-Moe & Nicolas (1977) that the C III, Si IV and C IV line profiles display wing emission significantly higher than the Doppler wings of the core profile. According to the detailed analysis made on the Si IV and C IV line profiles by Dere & Mason (1993), the enhanced wing indicates the existence of non-thermal motions at supersonic speeds. It is expected that enhanced wings exist also in the N V, S VI, and O VI lines formed at temperatures above 10^5 K in view of the fact that these lines display non-thermal velocities larger than those found in the Si IV and C IV lines. To investigate this possibility, we have examined the S VI λ933.38 line profile in detail. It should be noted that this line is especially suited for our purpose since it is well separated from other lines and has a low level of continuum. Recently Curdt & Schühle (1998) pointed out that the blending due to the He II λ933.44 line may be important in this S VI line. We estimated the intensity of the unresolved He II line by extrapolating the measured intensity of the He II λ958.724 line to the He II λ933.44 line (Curdt et al. 1997) using the H I Balmer decrement law presented by Allen (1973). The result gives $I(\mathrm{HeII})/(I(\mathrm{SVI}) + I(\mathrm{HeII}) = 0.02$. For safety reason, given the approximation, we can say that the He II line contribution is smaller than 0.05 of the total intensity, so we neglect this line contribution in the following discussion.

Figure 10 shows a typical S VI line profile which has been obtained by taking a $3''$ smoothing along the slit direction. An attempt was made to fit the profile by several different functional forms like a single Gaussian, two Gaussians, and a Voigt function. The single Gaussian profile which best fits the observed profile has been presented by the solid curves in Figure 10, which yields $\xi = 28$ km s^{-1}, about the same as the spatial average of non-thermal velocities. On the other hand, the Gaussian profile characterized by the FWHM value which has been simply estimated from the half maximum of the observed profile produces a significantly smaller value of 22 km s^{-1}. This difference results from the existence of enhanced wing, which affects the width determination using non-linear fitting. As seen from the figure, both the wing and the center of the observed profile can be much better fitted by employing either of a two-Gaussian or a Voigt function. Even though the Voigt function well fits the observed profile, this kind of fit seems to have no physical meaning in the transition region lines because the required damping parameter $a = 0.43$ can be realized only in the plasma with an electron density above 10^{18} cm^{-3} (Kjeldseth-Moe & Nicolas 1977), which is much greater than the observed transition region electron densities of 10^8-10^{11} cm^{-3} (See, for example, Mariska 1992). Since the line is neither optically thick nor collisionally broadened, it is likely that the enhanced wing of this line profile should be attributed to the existence of a high velocity component of non-thermal motion. Thus the two-Gaussian fit seems to be physically most meaningful. The result of the two-Gaussian fit indicates that this specific line profile is well explained by a combination of a high velocity component with $\xi = 50$ km s^{-1} and a low velocity component with $\xi = 15$ km s^{-1}

We examined the statistics of both the components in a quiet area of $100'' \times 100''$ and presented the results in Figure 11. Using a two-Gaussian fit we have measured integrated intensities of high velocity and low velocity components separately at every spatial point. The top panel in the figure shows the histogram of the intensity fraction of high velocity component, $I_{high}/(I_{high} + I_{low})$. The spatial average of the intensity fraction is found to be 0.23, which means that the high velocity component contributes only a small fraction to the total line intensity. This is the reason why it is not easy to discover high velocity components in the transition region lines. The low velocity component has an average ξ of 22 km s^{-1} with a standard deviation of 5 km s^{-1} and the high velocity component has an average of ξ of 55 km s^{-1} with a standard deviation of 19 km s^{-1}. It is noteworthy that the number distribution of the high velocity component ξ is highly asymmetric whereas the low velocity component ξ distribution is more or less normal. Also interesting is the existence of strong negative correlation between the intensity fraction and ξ the high velocity component as seen from the lower panel of the figure.

It seems worthwhile to compare high velocity components and explosive events (see, e.g., Dere 1994). These two kinds of features are similar to each other in that they are characterized by high velocities manifest in broad line profiles. Interestingly, the number distribution of ξ of the high velocity component monotonically extends over 100 km s^{-1}, a typical value of explosive events (see Figure 11). This suggests a possibility that explosive events may be an extreme tail of the high velocity component spectrum. This idea is also supported by the fact that they are observed at the similar temperature ranges, $6\times10^4 - 2\times10^5$ K. The main difference between explosive events and high velocity components is in the intensity fraction as seen from Figure 11. To illustrate this clearly, we have presented the S VI line profile of an explosive event in Figure 12. This event appears to be a rather weak one in that the profile shows not only the wide explosive component, but also the narrow stationary component. The profile has been fitted by a two-Gaussian, from which we find the non-thermal motion of about 90 km s^{-1} and intensity fraction of 0.67 in this explosive component. This intensity fraction is much higher than 0.1, a typical value in the high velocity components with $\xi = 90$ km s^{-1}. These comparisons suggest that high velocity components may be of the same physical nature as explosive events, but represent spatially unresolved events which occupy a much smaller fraction of either the emitting volume or the integration time than explosive events.

3.6. Exposure Time and Center-to-limb Dependence

It appears that the time scale of mass motions giving rise to non-thermal line broadening should be smaller than a few of tens seconds since our measurements show that the non-thermal motions do not depend significantly on exposure times. For example, the non-thermal velocities of the Si IV and C IV lines we obtained using the spectral data integrated over 400 and 500 seconds are about the same as the values determined from 20 second integration HRTS data by Dere & Mason (1993). We further examined this aspect using the C II λ1036.3 and O VI λ1037.6 lines from two sets of data having different exposures of 20 and 300 seconds. Results are give in Table 5. The C II line has no dependence on the exposure time. The O VI line has a little larger value of ξ in the longer exposure data with a difference of 4 km s^{-1}. If this difference could be attributed to the existence of an additional source of Doppler broadening, it should have a Maxwellian velocity distribution with a most probable line-of-sight component of about 16 km s^{-1}. Our examination of short exposure line profiles and long exposure profiles, however, shows that this difference is mainly reflecting the difference in the signal to noise ratio of the data used, which is especially important in revealing the extended wing parts of the line profiles, rather than the difference in the intrinsic line widths.

Whether the observed non-thermal motions are isotropic or not can be examined by comparing the disk center values with the values determined near limb. The near-limb non-thermal velocity of every line presented in Table 6, except the O I λ1355.6 and Mg X λ625.0 lines, is systematically 2 to 3 km s^{-1} larger than the disk center value. This requires an additional source of broadening with a most probable speed of 7-13 km s^{-1}. We have examined the intensity ratios as we did in the disk center observations and found that these lines all remain optically thin. Therefore the difference may not be due to opacity. An alternative explanation may be that a superposition of mass motions along the line of sight also contributes to the line width, resulting in a little greater value of non-thermal velocity in near-limb observation. Irrespective of its physical origin, the difference is so small that there is no difficulty in drawing a conclusion that the non-thermal motions are basically isotropic, confirming the previous results from Mariska, Feldman & Doschek (1978).

4. IMPLICATIONS FOR CORONAL HEATING MECHANISMS

It is expected that our results will shed a light on the physical nature of the non-thermal motions that give rise to EUV and FUV line broadening. We may consider three possibilities: 1) unresolved laminar flows, 2) waves, and 3) turbulent flows. Each should be closely associated with coronal heating mechanisms and will be examined in succession. We will also discuss the implication of our results for the nanoflare heating mechanism.

4.1. Unresolved Laminar Flows

Athay and Dere (1991b) suggested a scenario in which the dispersion in the peculiar flow velocities along different loops gives rise to the non-thermal line width where their mean gives rise to the line shift. This scenario is attractive in that it attempts to explain both the line width and line shift in the same context. If the non-thermal width of that value would result from a superposition of peculiar flow velocities along different loops, there should be a number of unresolved loops in the resolution element and they should have randomly distributed peculiar flow velocities which range from, for example, -50 to 50 km s^{-1} in the case of the C IV lines. There is increasing evidence of the existence of EUV and FUV emitting fine structures that are spatially unresolved (Feldman, Doschek & Mariska 1979; Dere et al. 1987; Athay & Dere 1991a). Furthermore, multiple velocities of about 30-50 km s^{-1} within a resolution element of 10^3 km have been frequently observed (Kjeldseth-Moe et al. 1994).

If unresolved loop flows are responsible for the non-thermal motion, several questions arising from our observational results need to be answered. First, our observation confirms that the non-thermal motions are isotropic at all the temperatures. This requires that the magnetic field direction should be randomly distributed at all the temperatures since unresolved loop flows are likely to be more or less along the loops. Second, the non-thermal velocity has a strong spatial correlation with intensity, and a low temperature non-thermal velocity has a strong correlation with a high temperature non-thermal velocity at least at temperatures $2 \times 10^4 - 1 \times 10^5$ K. Therefore unresolved loops should form a coherent macroscopic structure which displays these correlations. It is not easy, however, to imagine how the unresolved loops with different peculiar velocities can form such a structure because different peculiar velocities would imply different physical loop structures. Another difficulty in this hypothesis of unresolved loop flows comes from the fact that the non-thermal velocities estimated from the line widths are much larger than the Doppler shift values and their spatial fluctuations. Dere (1989) recognized the importance of this fact in revealing the physical nature of non-thermal motions. Based on the finding that the power in the unresolved velocity fluctuations inferred from line widths is much greater than that expected from a simple extrapolation of the power of the resolved velocity fluctuations inferred from line shifts, he suggested that the power of unresolved motions should be driven by some physical processes which are different from those giving rise to resolved Doppler shifts. A proper evaluation of this scenario will have to wait for a better understanding of unresolved fine structures.

4.2. Alfvén Waves

There have been many efforts to interpret the non-thermal motion in terms of either acoustic waves or MHD waves in connection with coronal heating (Boland et al. 1975; Mariska, Feldman & Doschek 1978; Cheng, Doschek, Feldman 1979; Hassler et al. 1990; Dere & Mason 1993). There are a couple of things which should be explained in an attempt to interpret non-thermal motions in terms of Alfvén waves. First, our observations indicate that if the non-thermal velocities are due to Alfvén waves, the waves should have a period shorter than a few tens of seconds. It is not certain whether such short period Alfvén waves can be effectively driven by mass motions in the convection zone and photosphere (Zirker 1993). Furthermore, the isotropic nature of the non-thermal motion is not easily explained by pure transverse Alfvén waves propagating in the field direction as in the case of loop flows because the dominating direction of the oscillatory motion in such waves should be perpendicular to the field direction.

It seems worthwhile to estimate the Alfvén wave energy flux based on our measurements of non-thermal velocities. According to Wentzel (1977) and Rosner et al.(1986), the energy flux density carried by Alfvén waves along the field direction is given by

$$F_A = \rho \langle v_\perp^2 \rangle v_A, \tag{6}$$

where $\langle v_\perp^2 \rangle$ is the dispersion of wave motion perpendicular to the field direction, which becomes equal to ξ^2, the square of the most probable speed in the direction of the line of sight due to the isotropic nature of the non-thermal motions. v_A is the Alfvén speed given by $v_A = \sqrt{B/4\pi\rho}$. Some authors have used a factor of $3/2$ in Equation 6 because they have considered that all the three velocity components will contribute to the energy transport. In a pure Alfvén wave, however, only those oscillating components perpendicular to the propagating direction contribute to the energy transport.

It is clear that the upper solar atmosphere is highly inhomogeneous with physical parameters such as density and magnetic field strength varying much from region to region. In principle, to calculate the wave flux density averaged over the solar surface, we need to calculate the flux density at every position on the Sun and then take a spatial average. However, we lack a detailed knowledge of such spatial fluctuations which need to be known at spatial scales smaller than $1''$. Therefore, spatially averaged quantities will be used for the energy flux calculation. In the present study, we already produced the spatially averaged non-thermal motions as a function of temperature. The temperature dependence of the spatially averaged density can be obtained under the assumption of constant pressure in the transition region and corona. Measurements of electron density in the quiet Sun have shown that the typical pressure in the transition region is about 0.3 dyn cm^{-2} (Mariska 1992). We use 8 G as a typical magnetic field strength at the transition region heights of 2000-4000 km. The value has been inferred from the potential extrapolation of a quiet Sun magnetogram obtained at Big Bear Solar Observatory.

In Figure 13, the quiet Sun Alfvén wave flux determined from the observed non-thermal velocities has been shown as a function of temperature. To aid in calculation, we have used a polynomial of 3rd order which best fits the observed variation of non-thermal velocities presented in Figure 5. The Alfvén wave flux is compared with the integrated radiative loss

$$R(T) = \int_T^\infty \Lambda(T')\mathrm{DEM}(T')dT', \tag{7}$$

calculated by Dere & Mason (1993) using their own estimate of the differential emission measure,DEM, and the radiative loss rate, Λ of Cook et al. (1989). As seen from the figure, the Alfvén wave flux inferred from the non-thermal velocities appears abundant and enough for the integrated radiative loss at temperatures above 3×10^4 K. We also find that at temperatures below 3×10^4 K the wave flux is much smaller than the integrated radiative loss and rapidly increases with temperature. This is a direct result of the behavior of the non-thermal motions at those temperatures. A similar trend was also noted by Boland et al. (1975) and Mariska et al. (1978). If this behavior of the flux at the low temperatures is real, it would be opposed to Alfvén waves propagating upward from the low temperature region to the high temperature region since the flux of such waves is expected to remain constant or decrease as temperature increases. However our present knowledge on cooler line formation and transition region magnetic field is so limited that it is difficult to draw any conclusion as yet.

4.3. MHD Turbulence

The interpretation of non-thermal motions in terms of turbulence is attractive in several respects. First of all, non-thermal motions display some observational characteristics which are consistent with turbulent motions: non-thermal motions are isotropic and have very small scales. Second, the physical conditions in the transition region and corona are suitable for the existence of turbulence. The extremely small values of molecular viscosity and magnetic diffusivity make the inertial force dominate over resistive forces, allowing mechanical energy to cascade from large scales to small scales. The inhomogeneous structures caused by density stratification and the magnetic field may also play a role in driving turbulence. Finally, most of the present coronal heating theories require the existence of turbulence because it is very difficult to dissipate mechanical energy without it (e.g., Hollweg 1984). In the following, we are going to examine the implications of the observed non-thermal velocities for turbulent coronal heating mechanisms.

Recently, several attempts were made to explain coronal heating in terms of steady state MHD turbulence in the corona driven by photospheric motions (Gómez & Ferro Fontán 1988, 1992; Heyvaerts & Priest 1992). According to Gómez & Ferro Fontán (1988), there may be three different regimes in MHD turbulence depending on the relative importance of velocity and magnetic fields: 1) dynamic alignment (equipartition between kinetic energy and magnetic energy), 2) Navier-Stokes (kinetic energy is dominant), and 3) selective decay (magnetic energy is dominant). Since turbulent magnetic fields have never been measured in the transition region or corona, it is difficult to determine to which regime the MHD turbulence in the solar corona belongs. Here we examine the two cases of dynamic alignment and selective decay which have been considered by Heyvaerts & Priest (1992) and Gómez & Ferro Fontán (1988), respectively.

In the turbulent regime dominated by the dynamic alignment, there is an equipartition between kinetic energy and magnetic energy. Both the kinetic energy and the magnetic energy of three-dimensional isotropic MHD turbulence in this regime follow the Kraichnan spectrum (Kraichnan 1965)

$$E(k) = C\sqrt{\epsilon v_A}\, k^{-3/2}. \tag{8}$$

Here, ϵ is the energy injection rate per mass which should be equal to the heating rate per unit mass. The dimensionless number, C, is a constant whose value was taken to be 0.9 by Heyvaerts & Priest (1992). By integrating the spectrum over the inertial range we get

$$\frac{1}{2}\langle v^2\rangle = 2C\sqrt{\epsilon v_A/k_{min}} \tag{9}$$

which gives the heating rate ϵ

$$\epsilon = \epsilon_{kr} k_{min}\xi^4/v_A \tag{10}$$

in terms of the non-thermal velocity ξ. Here we have used the relation $\langle v^2\rangle = \frac{3}{2}\xi^2$. The dimensionless constant ϵ_{kr} replaced $\frac{9}{64C^2}$ and has the value of 0.17. The quantity k_{min} is the smallest wave number where mechanical energy is injected. We do not have any way to fix k_{min} based on either prior observations or theoretical considerations, so it will be treated as a free parameter in the following discussion.

On the other hand, Gómez & Ferro Fontán (1988, 1992) argued, based on the small value of the ratio α of a typical Alfvén wave travel time along a coronal loop to a characteristic time of subphotospheric motions, that the turbulence in the corona should be in the regime of selective decay. They found that the total energy in two-dimensional MHD turbulence dominated by selective decay follows the Kolmogorov spectrum

$$E(k) = \pi(\epsilon/2\alpha)^{2/3}\, k^{-5/3}. \tag{11}$$

If we assume that the kinetic energy spectrum has the same shape as the total energy spectrum with a ratio of β, we can derive the heating rate ϵ in terms of turbulent velocity as

$$\epsilon = \epsilon_{ko} k_{min} \xi^3. \tag{12}$$

The dimensionless constant ϵ_{ko} is equal to $\frac{2\alpha}{(2\pi\beta)^{3/2}}$ where β is the ratio of the kinetic energy to the total mechanical energy. Gómez and Ferro Fontán (1988, 1992) estimated $\alpha \simeq \beta \simeq 0.04$ so that $\epsilon_{ko} = 0.63$. Hollweg (1984) postulated essentially the same formula as Equation 12 for the case of a two-dimensional turbulent rolls which follows a hydrodynamic Kolmogorov spectrum in the inertial range. Interestingly his order-of-magnitude estimate of a dimensionless constant appearing in the energy spectrum leads to $\epsilon_{ko} = 0.54$ which happens to be close to the above value.

We are going to determine the free parameter k_{min} from the requirement that the radiative loss and turbulent heating should be globally balanced throughout the transition region and corona. We do not consider any energy transport process like thermal conduction and enthalpy flow in this global energy balance because such processes play only the role of redistributing thermal energy and have no net effects in the global energy balance. The energy loss through solar wind may affect the global energy balance especially in coronal holes, but we neglect it in the present consideration since we are dealing with the normal quiet Sun without coronal holes. The global balance at temperatures above T_0, therefore, means that the radiative loss integrated above T_0 should be equal to the turbulent heating integrated over the same temperature range, i.e.,

$$H(T_0) = R(T_0) \tag{13}$$

where the integrated heating rate is defined in a similar way as in Equation 7

$$H(T_0) = \int_{T_0}^{\infty} \rho\epsilon(T') \frac{\mathrm{DEM}(T')}{n_e n_H} dT'. \tag{14}$$

By choosing $T_0 = 2 \times 10^4$K, we have determined in each case of the turbulence spectrum a value of the free parameter k_{min} or equivalently, its corresponding injection scale length $l \equiv 2\pi/k_{min}$.

The determined values of the scale length are 15 km for a Kraichnan type turbulence (Equation 10) and 1200 km for Kolmogorov type turbulence (Equation 12). What is found from the comparison of these scale lengths is that Kolmogorov type turbulence is more preferred in coronal heating than Kraichnan type turbulence. The injection scale length of the Kolmogorov type turbulence 1200 km is of the order of photospheric granulation size and of the order of the transition region line emission FWHM size (e.g., Dere et al. 1987), so it appears to be physically plausible. On the other hand, for case of the Kraichnan type turbulence, the energy should be injected at a much smaller scale of 15 km, which is far below the resolution limit.

4.4. Nanoflare Heating

The existence of high velocity components in the transition region line profiles is another important observational clue to a better understanding of MHD turbulence in coronal loops and its implications for coronal heating. According to recent numerical studies (Hendrix & Van Hoven 1996; Dmitruk & Gomez 1997), the development of MHD turbulence in coronal loops driven by footpoint motions is coincident with the formation of a coherent structure consisting of a current sheet and an Alfvénic plasma outflow, indicating that MHD turbulence and small scale magnetic reconnection are closely connected to each other. The formation and development of this coherent structure occupying only a small fraction of the total volume occurs intermittently and results in a succession of impulsive heating. Dmitruk & Gomez (1997) identified these impulsive events with nanoflares proposed by Parker (1988) and showed their number distribution agrees well with the empirical distribution obtained from flare events.

We find that the non-thermal motions in the high velocity components display several characteristics which are expected from nanoflares. First, it has been shown that high velocity events are similar to explosive events. Now there has been increasing evidence that explosive events are a manifestation of magnetic reconnections occurring in the transition region (Dere et al. 1991; Dere 1994; Innes et al. 1997; Chae et al. 1998), so it is likely that high velocity components also represent magnetic reconnection and associated turbulence occurring in unresolved scales. Second, the observed average non-thermal velocity values of high velocity components are in the range of 30-50 km s^{-1}, which is compatible with values theoretically expected in loops with nanoflares. (Dmitruk & Gomez 1997). Finally the ratio of high velocity component intensity to the total line intensity is much smaller than unity. This may indicate that the non-thermal motions appearing as high velocity components are occupying only a small fraction of either the volume or the exposure time, which is consistent with the intermittent characteristics of nanoflares.

It appears that high velocity components are important in coronal heating at the temperatures where they are found. First, high velocity components may be more important than explosive events because they are much more commonly seen. Even though explosive events in the Sun are quite common, they occupy only a small fraction of the solar surface so that it still poses a problem in explaining heating in the region where these events are not found. High velocity components, on the other hand, appear to exist everywhere in the solar surface. Therefore they may be dominating over explosive events as far as heating is concerned. Second, the contribution of high velocity components to heating overwhelms both that of low velocity non-thermal motion and that of non-thermal motions determined from the single Gaussian fitting. This is because the turbulent heating rate is proportional to a high power of non-thermal velocity. For example, if we assume Kolmogorov spectrum, the heating rate is proportional to $f\xi^3$ where f is the volume filling factor which we set to be equal to 0.25 in the high velocity component and 0.75 in the low velocity component based on the observed intensity ratios. Therefore the heating rate of the high velocity component with $\xi = 55$ km s^{-1} is about 5 times that of the low velocity component with $\xi = 22$ km s^{-1}. Similarly the sum of two component heating rates is about 1.7 times the value we already estimated using the single component with $\xi = 29$ km s^{-1}. If we assume Kraichnan spectrum, these ratios have even larger values of 13 and 3.2, respectively.

5. SUMMARY AND CONCLUSION

In the present work, we have measured non-thermal velocities in the transition region and corona of the quiet Sun by measuring the widths of a number of EUV and FUV lines taken with SUMER. The line widths were determined by applying to the observed line profiles non-linear iterative Gaussian fittings which take into account the photon noise characteristics of the SUMER data. The width of the instrumental profile was estimated from the narrowest width of the O I λ1355.6 line obtained in a quiet region and has the FWHM value of 2.3 detector pixels for the observations taken with the use of the A detector. The observations using the B detector have a poorer spectral resolution of 2.6-3.6 detector pixels. It was shown that opacity severely affects the widths of most of the lines emitted by neutrals and singly ionized atoms except the lines O I $\lambda\lambda$1355.6/1358.5, C I λ1315.9, N I λ1319.7, S II λ1253.8. Even though the C II $\lambda\lambda$1036.3/1037.0 lines are broadened by the opacity, we have used these lines for the determination of non-thermal velocity around $T = 3 - 4 \times 10^4$ K after the correction of the opacity effect. Other lines emitted from highly ionized atoms turn out optically thin in disk observations.

Most of our width measurements came from disk observations of the quiet Sun. The non-thermal velocity is smaller than 10 km s^{-1} at temperatures below 2×10^4 K, increases with temperature, has a peak value of 30 km s^{-1} around 3×10^5 K, and then decreases with temperature having a coronal temperature value of about 20 km s^{-1}. The spatial fluctuation in the quiet Sun results mainly from the network-cell structure and has the rms value of 3-5 km s^{-1} at temperatures $3 \times 10^4 - 3 \times 10^5$ K. There exists a strong correlation between intensity and non-thermal velocity at temperatures $2 \times 10^4 - 1 \times 10^5$ K and the correlation at higher temperatures weakens as temperature increases. The correlation between the non-thermal velocities of a set of any two lines with temperatures below $1 - 2 \times 10^5$ K is relatively strong, but the non-thermal velocity at a higher temperature is weakly correlated with that at these temperatures. Neither significant center-to-limb change nor meaningful dependence on the integration time was found from the measured non-thermal motions, which means that the non-thermal motion is essentially isotropic and remains unresolved at a spatial resolution of about 1000 km and at a time resolution of about a few tens of seconds. We have discovered an existence of high velocity components in the observed profiles of the S VI line formed around 2×10^5K. The average non-thermal velocity and intensity fraction of the S VI line high velocity components are found to be 55 km s^{-1} and 0.25, respectively. Interestingly the non-thermal velocity has a strong negative correlation with the intensity fraction and has a number distribution which is far from the normal distribution and monotonically extends over to the velocities of explosive events.

We have considered several MHD processes proposed to explain the non-thermal motions manifest in the line widths, especially in connection with the coronal heating problem. The principle of the superposition of unresolved loop flows with different peculiar velocities tries to explain both the width and shift of a line in the same context, but it is not clear how this idea can explain some observational characteristics of non-thermal motions such as isotropic nature, spatial correlations, and the fact that non-thermal velocities manifest in line widths are much larger than the spatial averages and fluctuations of line shifts. If the observed non-thermal motions are a manifestation of Alfvén waves, the wave periods should be shorter than a few tens of seconds. The Alfvén wave energy flux density inferred from the measured non-thermal velocities appears abundant and enough for the radiative loss throughout the transition region and corona at temperatures above 3×10^4 K. There is a tendency that the fluxes below 3×10^4 K are much smaller than the fluxes at higher temperatures.

The isotropic and small scale nature of the non-thermal motions appear to be suited for MHD turbulence. If the non-thermal motions represent MHD turbulence following a Kolmogorov spectrum, the turbulent heating rates inferred from the non-thermal velocities can successfully account for the radiative loss throughout the transition region and corona by picking up a mechanical energy injection scale length of about 1000 km. A Kraichnan type turbulence is less preferred than Kolmogorov type turbulence because it requires much smaller scale length of 15 km to explain the coronal heating. It is likely that the high velocity components found in the profiles of the Si IV, C IV, and S VI lines are a manifestation of unresolvable scale magnetic reconnection and associated MHD turbulence. The turbulent heating inferred from the high velocity components appears as a dominant heating mechanism, at least at these line forming temperatures $6 \times 10^4 - 2 \times 10^5$ K, supporting Parker (1988)'s nanoflare picture. It will be important to determine whether high velocity component non-thermal motions exist also at higher temperatures.

We would like to thank H.S. Yun, Klaus Wilhelm and Haimin Wang for their valuable comments. We also thank Carsten Denker, Scot Kleinman and Martin Woodard for careful manuscript reading. We are indebted to the referee's good comments and useful suggestions for improving this paper. One of us (J. Chae) is grateful to Arthur Poland for kind encouragement. A part of this work was done during his stay at Goddard. This work is partially supported by NSF under grant ATM-9628862 and NASA under grant NAG5-3536 to BBSO. The SUMER project is financially supported by DLA, CNES, NASA, and the ESA PRODEX programme (Swiss contribution).

REFERENCES

Allen, C. W. 1973, Astrophysical Quantities, University of London

Arnaud, M & Rothenflug, R. 1985, A&AS, 60, 425

Athay, R. G. & Dere, K.P. 1991a, ApJ, 379, 776

Athay, R. G. & Dere, K. P. 1991b, ApJ, 381, 323

Athay, R. G., Gurman, J. B., Henze, W., & Shine, R. A. 1983, ApJ, 265, 519

Athay, R. G. & Judge, P. G. 1995, ApJ, 438, 491

Athay, R. G. & White, O. R. 1980, ApJ, 240, 306

Boland, B. C., Dyer, E. P., Firth, J. G., Gabriel, A. H., Jones, B. B., Jordan, C., Mcwhirter, R. W. P., Monk, P., & Turner, R. F. 1975, MNRAS, 171,697

Bruner, E. C., Jr. & Mcwhirter, R. W. P. 1979, ApJ, 231, 557

Carlsson, M. & Judge, P. G. 1993, ApJ, 402, 344

Chae, J. , Yun, H. S., & Poland, A. I. 1998, ApJS, 114,151

Chae, J., Wang, H., Lee, C.-Y., Goode, P. R., & Schühle, U. 1998, ApJ, in publication

Cheng, C.-C., Doschek, G. A., & Feldman, U. 1979, ApJ, 227, 1037

Cook, J. W., Cheng, C.-C., Jacobs, V. L., & Antiochos, S. K. 1989, ApJ, 338, 1176

Curdt, W., Feldman, U., Laming, J. M., Wilhelm, K., Schühle, U., & Lemaire, P. 1997, A&AS, 126, 281

Curdt, W. & Schühle, 1998, private communication

Dere, K. P. 1989, ApJ, 340, 599

Dere, K. P., Bartoe, J.-D. F.,& Brueckner, G. E. 1984, ApJ, 281,870

Dere, K. P., Bartoe, J.-D. F., Brueckner, G. E., Cook, J. W., & Socker, D. G. 1987, Solar Phys., 114, 223

Dere, K. P., Bartoe, J.-D.F., Brueckner, G.E., Ewing, J. & Lun, P. 1991, JGR, 96, 9399

Dere, K. P. & Mason, H. E. 1993, Solar Phys., 144, 217

Dere, K. P. 1994, Adv. Space Res. 14, 413

Dmitruk, P & Goméz, D. O. 1997, ApJ, 484, L83

Doschek, G. A., Feldman, U., Van Hoosier, M. E., & Bartoe, J.-D. F. 1976, ApJS, 31, 417

Doschek, G. A., Mariska, J. T., & Feldman, U. 1981, MNRAS, 195, 107

Doyle, J. G., O'shea, E., Erdélyi, R., Dere, K. P., Socker, D. G., & Keenan, F. P. 1997, Solar Phys., 173, 243

Feldman, U., Doschek, G.A., & Mariska, J.T. 1979, ApJ, 229, 369

Feldman, U., Doschek, G.A., & Patterson, N.P. 1976, ApJ, 209, 270

Gómez, D.O., & Ferro Fontán, C., 1988, Solar Phys., 116,33

Gómez, D.O., & Ferro Fontán, C., 1992, ApJ, 394, 663

Hendrix, D. L. & Van Hoven, G. 1996, ApJ, 467, 887

Hassler, D. M., Rottman, G. J., Shoub, E. C., & Holtzer, T. E. 1990, ApJ, 348, L77

Heyvaerts, J. & Priest, E. R. 1992, ApJ, 390, 297

Hollweg, J. V., 1984, ApJ, 277, 392

Innes, D. E., Inhester, B., Axford, W. I., & Wilhelm, K. 1997, Nature, 386, 811

Inverarity, G. W., & Priest, E. R. 1995a, A&A, 296, 395

Inverarity, G. W., & Priest, E. R. 1995b, A&A, 302, 567

Inverarity, G. W.,Priest, E. R., & Heyvaerts, J. 1995, A&A, 293, 913

Ionson, J. A. 1982, ApJ, 254, 318

Kjeldseth-Moe, O. & Nicolas, K. R. 1977, ApJ, 211, 579

Kjeldseth-Moe, O., Brynilden, N., Brekke, P., & Maltby, P. 1994, Space Science Rev. 70, 89

Kraichnan, R. H., 1965, Phys. Fluids, 8, 138

Lemaire, P., Wilhelm, K., Curdt, W., Schühle, U., Marsch, E., Poland, A. I., Jordan, S. D., Thomas, R. J., Hassler, D. M., Vial,J.-C., Kühne,M., Huber,M.C.E., Siegmund, O. H. W., Gabriel, A., Timothy, J. G., & Grewing, M. 1997, Solar Phys.,170, 105

Mariska, J.T. 1992, The Solar Transition Region, Cambridge Univ. Press

Mariska,J.T., Feldman, U., & Doschek, G.A. 1978, ApJ, 226, 698

Ofman, L., Davila, J.M., & Steinolfson, R.S. 1995, ApJ, 444, 471

Parker, E. N. 1983a, ApJ, 264, 635

Parker, E. N. 1983b, ApJ, 264, 642

Parker, E. N. 1988, ApJ, 330, 474

Poedts, S., Goossens, M., & Kerner, W. 1990, ApJ, 360, 279

Rosner, R., Low, B. C., Holzer, T. E. 1986, Physics of the Sun, Vol II. p.135, ed. Sturrock, P.A., D. Reidel Publishing Company

Seely, J. F., Feldman, U., Schühle, U., Wilhelm, K., Curdt, W., & Lemaire, P. 1997, ApJ, 484, L87

Wentzel, D. G. 1977, Solar Phys., 52, 163

Wilhelm, K., Curdt, W., Marsch, E., Schühle, U., Lemaire, P., Gabriel, A., Vial, J.-C., Grewing, M., Huber, M. C. E., Jordan, S. D., Poland, A. I., Thomas, R. J., Kühne, M., Timothy, J. G., Hassler, D. M., Siegmund, O. H. W. 1995, Solar Phys., 162, 189

Wilhelm, K., Lemaire, P., Curdt, W., Schühle, U., Marsch, E., Poland, A. I., Jordan, S. D., Thomas, R. J., Hassler, D. M., Huber, M. C. E., Vial, J.-C., Kühne, M., Siegmund, O. H. W., Gabriel, A., Timothy, J. G., Grewing, M., Feldman, U., Hollandt, J. G., & Brekke, P. 1997, Solar Phys., 170,75

Vernazza, J. E., Avrett, E. H., & Loeser, R. 1981, ApJS, 45, 635

Zirin, H. 1988, Astrophsyics of the Sun, p. 95, Cambridge University Press

Zirker, J. B. 1993, Solar Phys., 148, 43

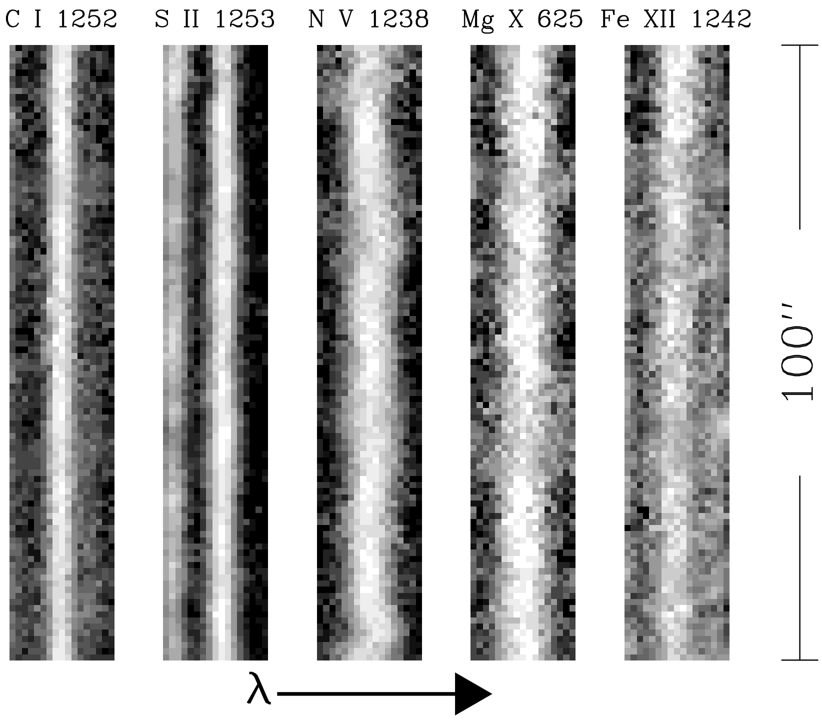

Fig. 1.— An illustration of a few EUV and FUV line spectrograms which were taken from a slit image of a quiet region to demonstrate the temperature dependent spectral characteristics of the same region. Note that each row of a line spectrum image, namely, the line spectral profile at a spatial point has been normalized by the integrated intensity of the line at the point for the purpose of making it easy to examine the spatial variation of the line width.

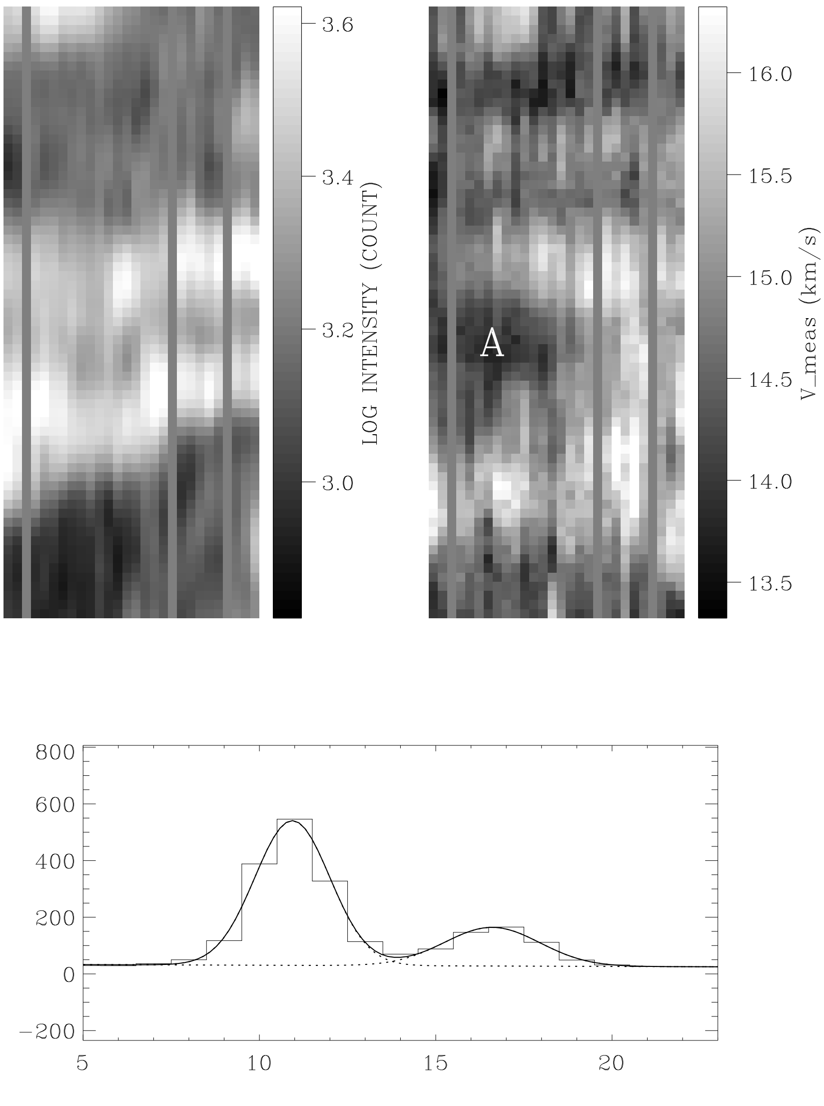

Fig. 2.— Top : O I λ 1355.6 line intensity (left) and width (right) maps around the point A which displays the minimum line width. The field of view is $32'' \times 66''$. Bottom : A two-Gaussian fit of the O I λ 1355.6 and C I λ 1355.8 lines at the point A. Here one detector pixel corresponds to 43 mÅ or 9.5 km s^{-1}.

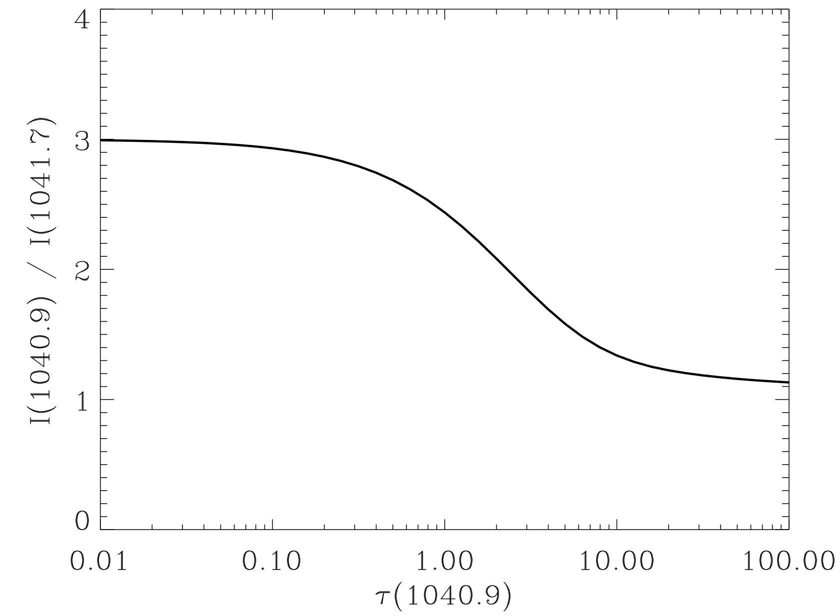

Fig. 3.— Theoretical intensity ratio of O I λ1040.9 to 1041.7 line as a function of the optical depth at the center of O I λ1040.9 line.

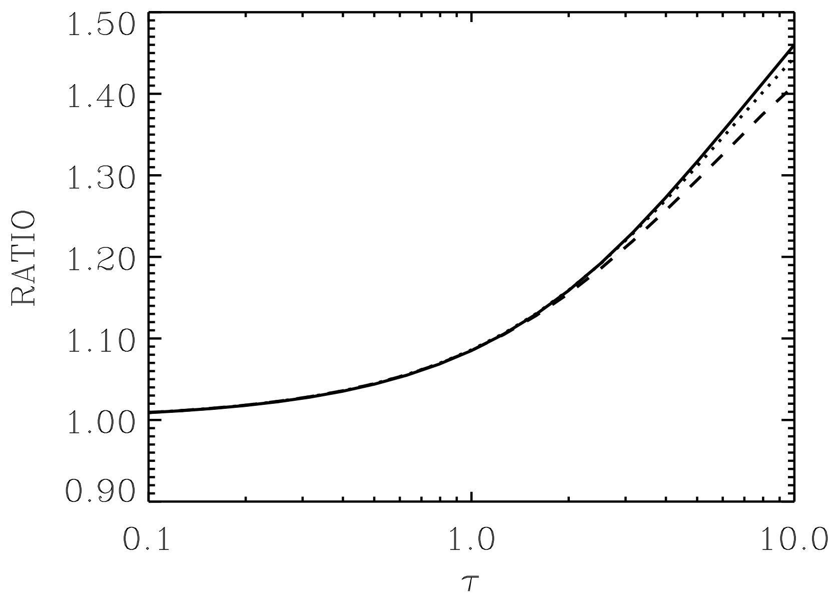

Fig. 4.— The ratios of solar broadening v_{solar} to $\sqrt{2kT/M+\xi^2}$ as functions of opacity presented in the three cases of $\sqrt{2kT/M+\xi^2}/v_{ins}$ =0.5 (solid curves), 1.0 (dotted curve) and 2.0 (dashed curve).

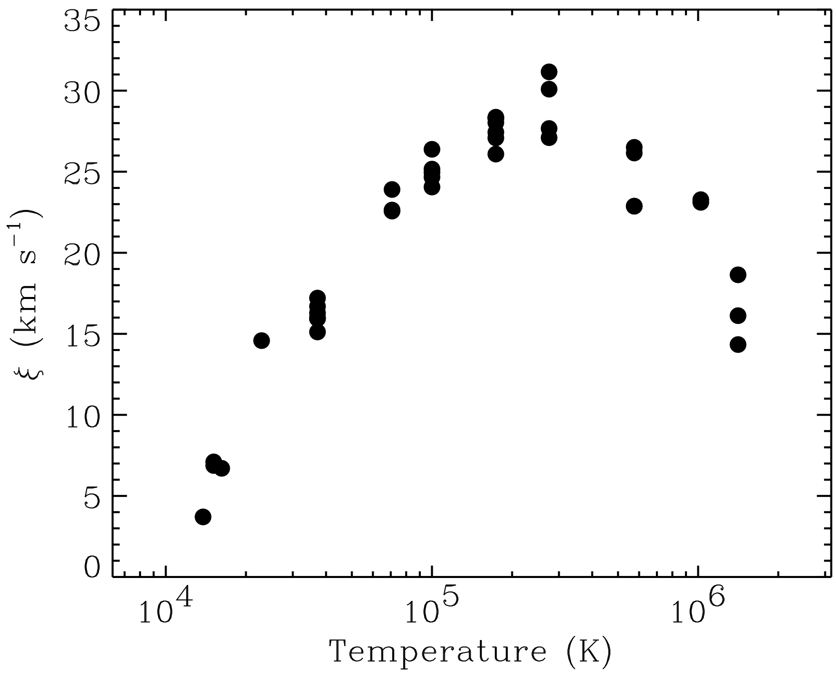

Fig. 5.— Non-thermal velocities versus temperature for the quiet Sun.

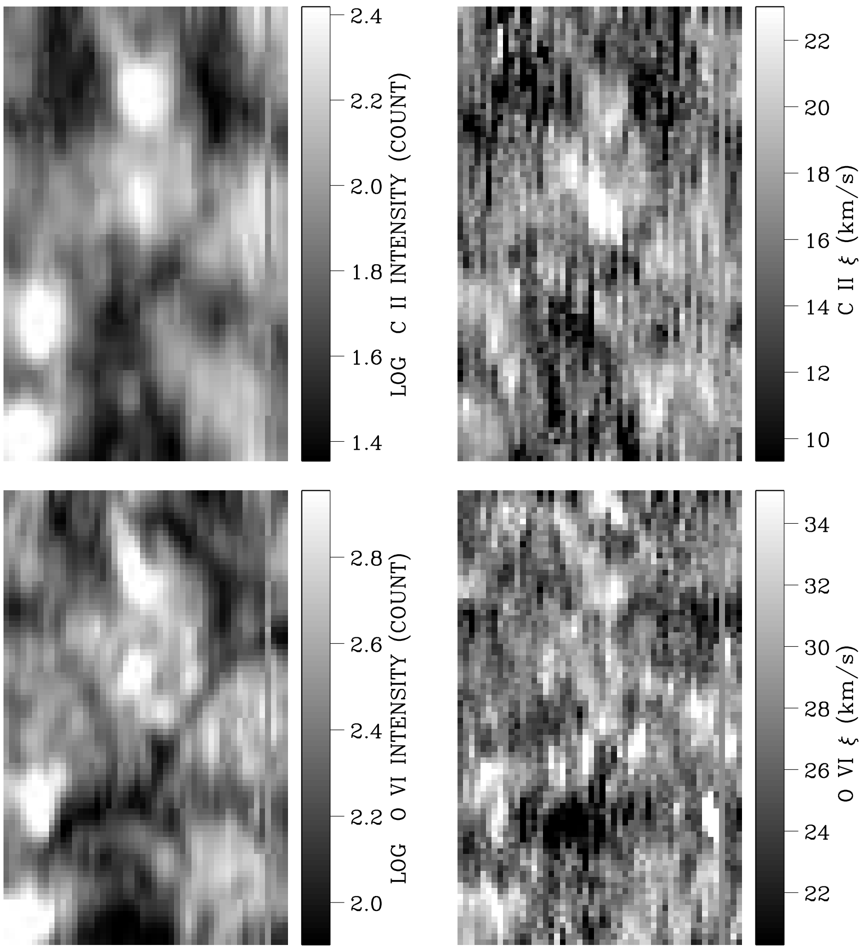

Fig. 6.— Integrated intensity and non-thermal motion maps of the C II λ1036.3 and O VI λ1037.6 lines in a quiet region. The field-of-view is $50'' \times 80''$.

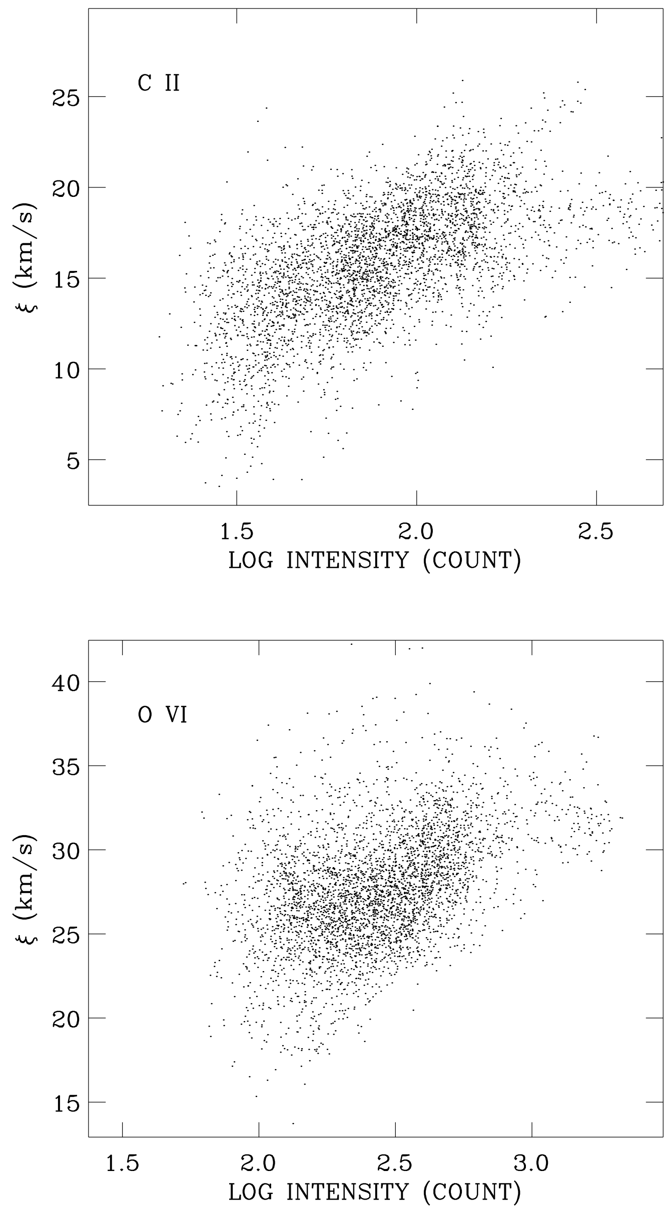

Fig. 7.— Plots of ξ versus logarithmic intensity for the C II λ1036.3 and O VI λ1037.6 lines in the region displayed in Figure 6.

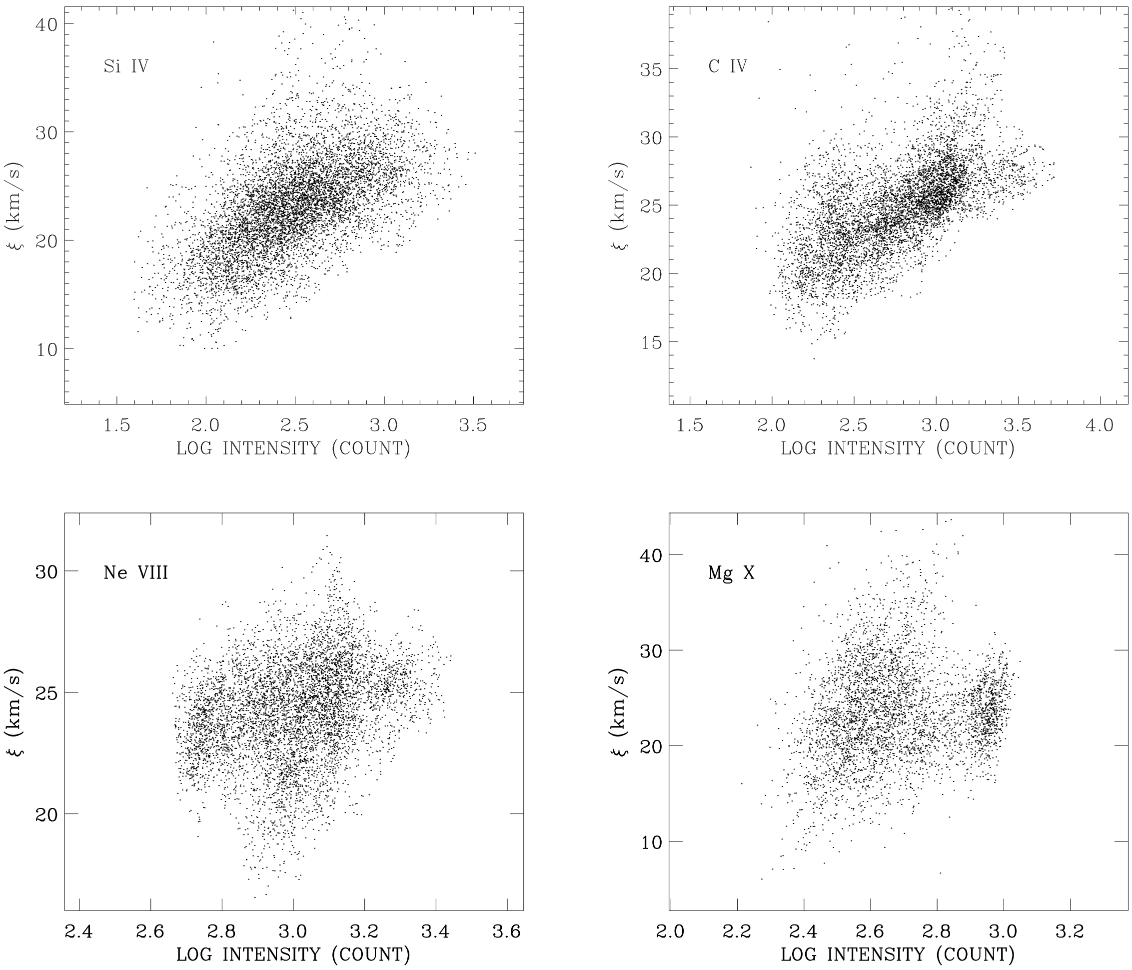

Fig. 8.— Plots of ξ versus logarithmic intensity for the Si IV $\lambda1393.8$, C IV $\lambda1548.2$, Ne VIII $\lambda770.4$ and Mg X $\lambda625.0$ lines in quiet Sun regions.

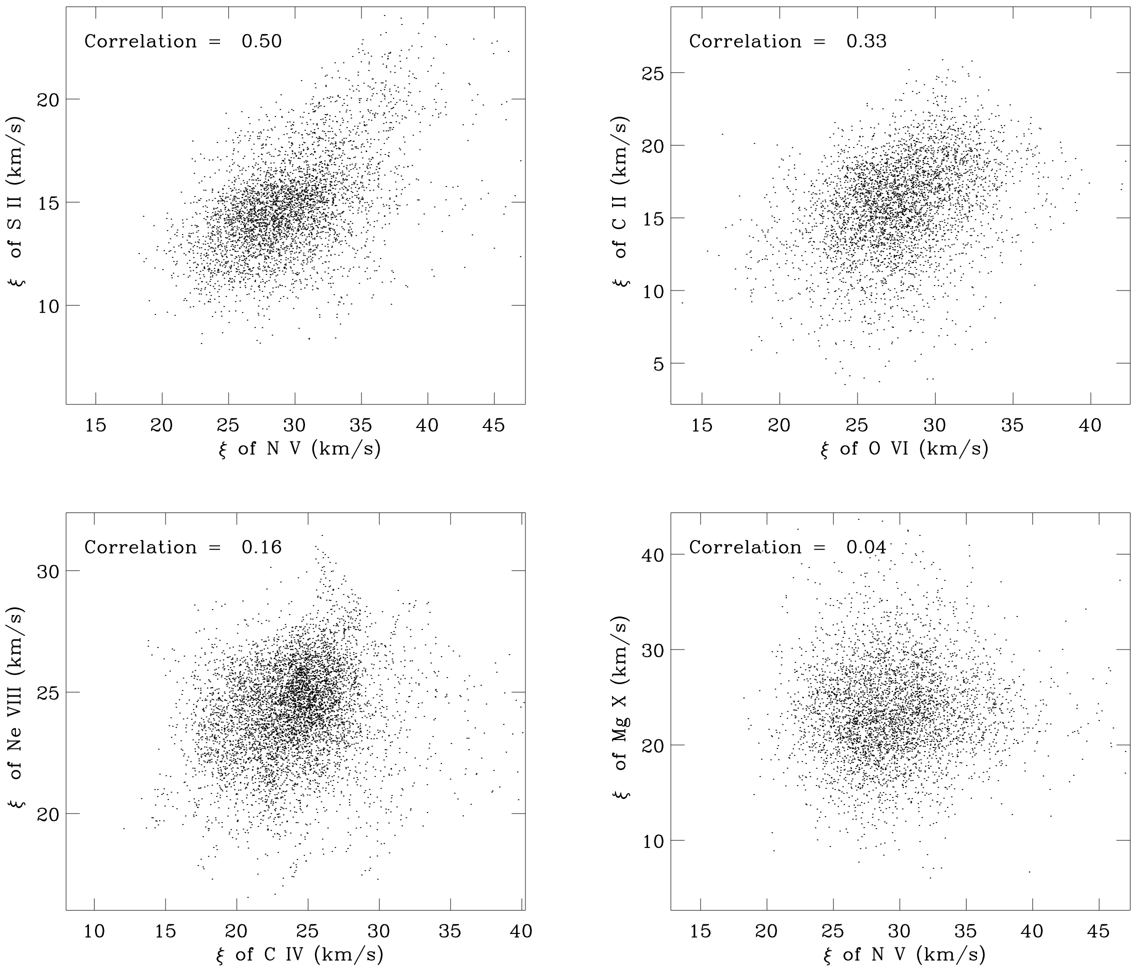

Fig. 9.— Correlations of ξ between the lines with different formation temperatures

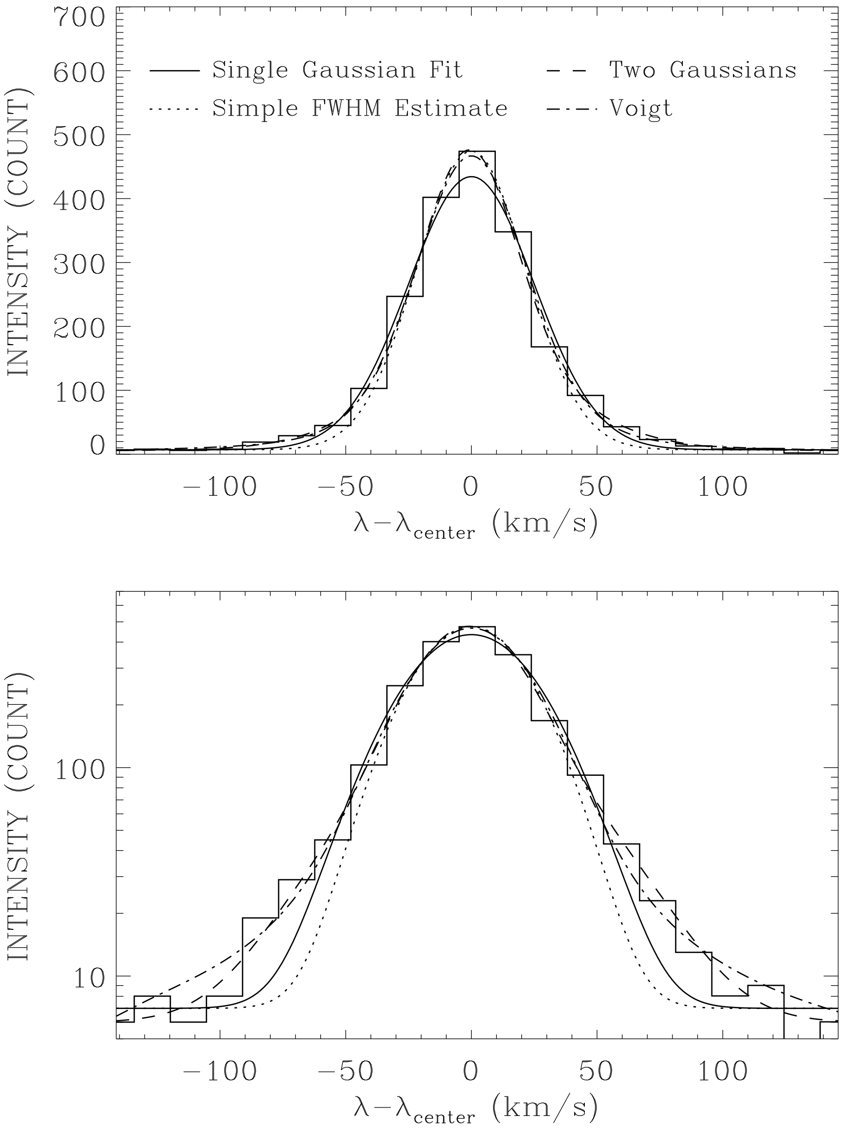

Fig. 10.— An example of the S VI 933 Å line profile of a quiet region (upper panel: linear scale, lower panel: logarithmic scale).

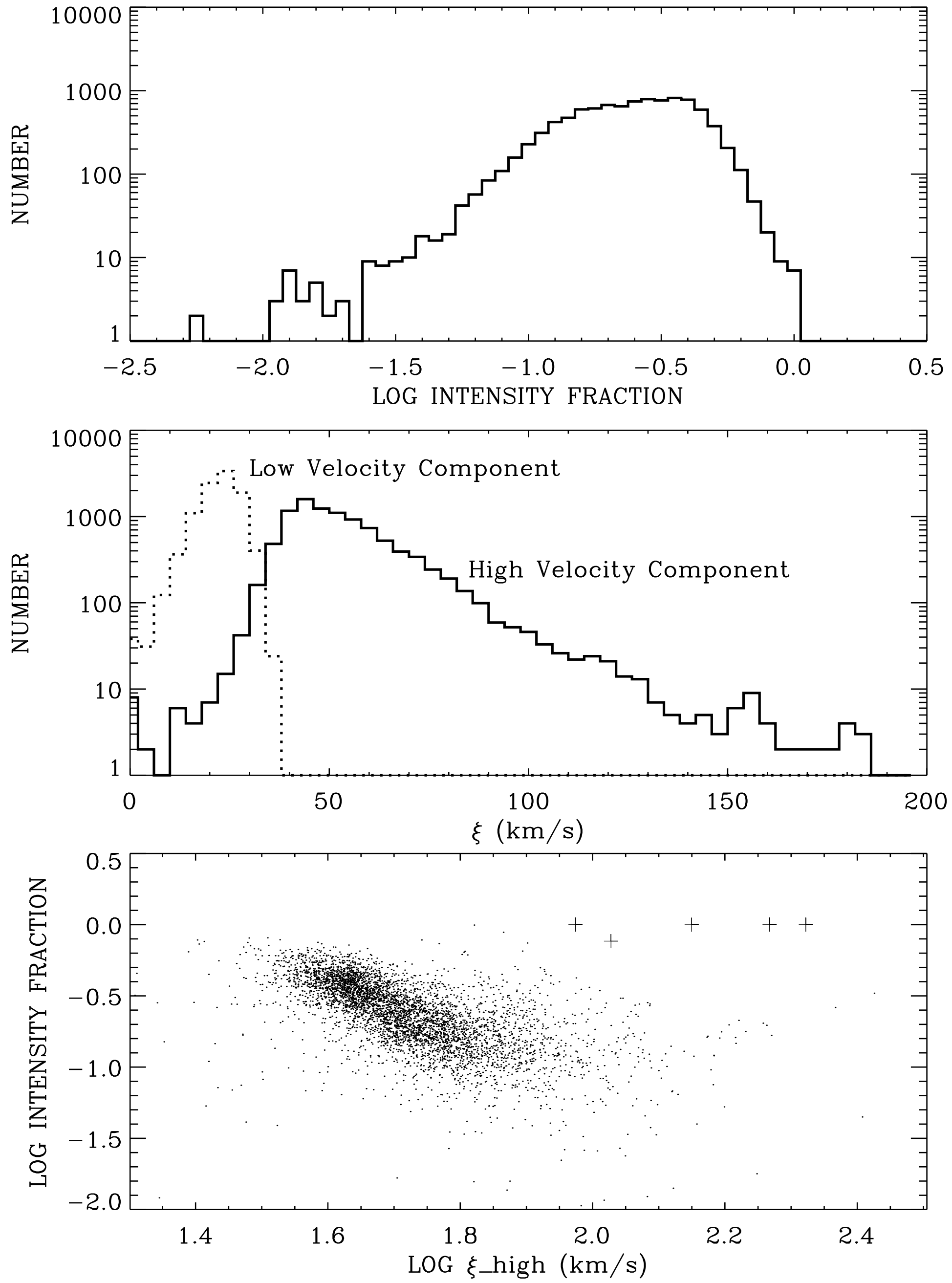

Fig. 11.— Top: the number distribution of the intensity fraction of high velocity component in the S VI λ933.4 line profiles. Middle: the number distributions of the low and high velocity component non-thermal velocities. Bottom: Plot of intensity fraction versus non-thermal velocity of high velocity component. Several data points marked by + represent explosive events.

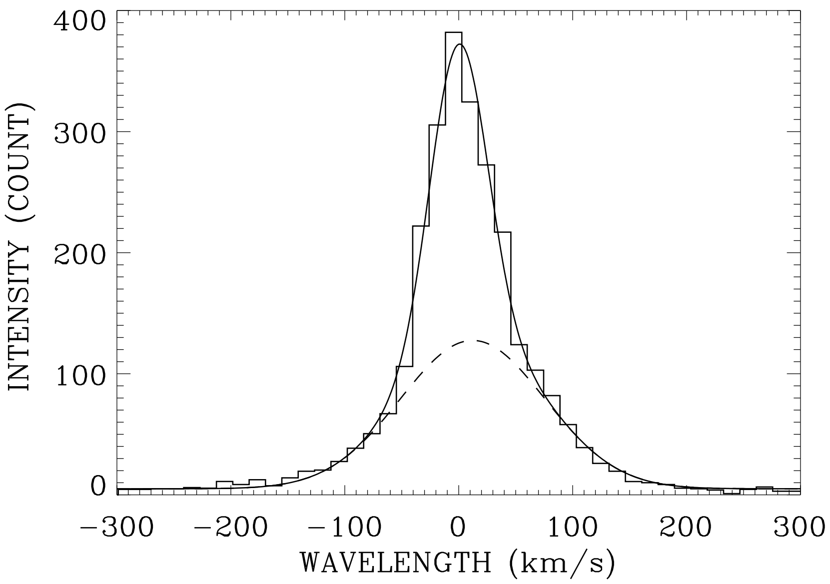

Fig. 12.— A two-Gaussian fit of an explosive event profile displaying both the wide explosive component and narrow stationary component.

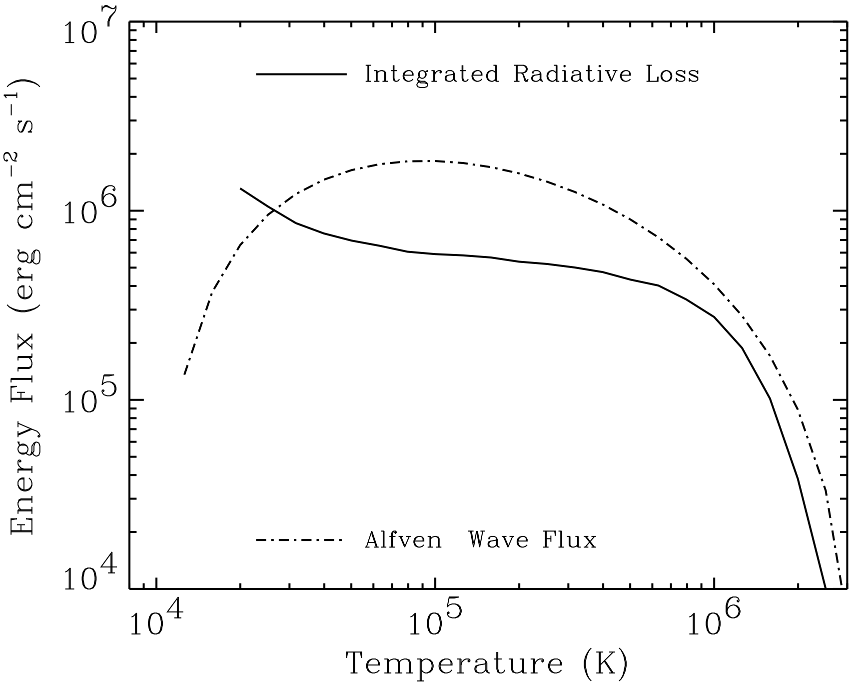

Fig. 13.— Comparison of computed Alfvén wave flux with integrated radiative loss rate.

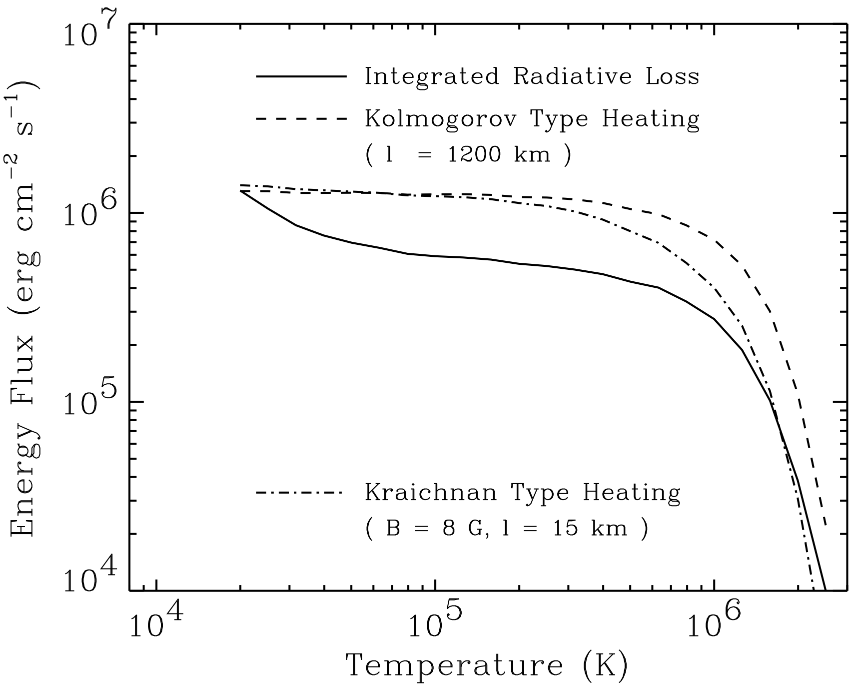

Fig. 14.— Comparison of integrated turbulent heating rate with integrated radiative loss rate.

Table 1: Width measurements of the narrowest neutral lines taken from 3 through 5 August 1996. The instrumental broadening (FWHM) of 2.3 detector pixels has been used for the calculation of the solar broadenings.

Line	log T (K)	v_{meas} (km s^{-1})	v_{solar} (km s^{-1})	Obs Time[a]	Det/Slit	FOV ($''$)	Exp (s)
Cl I λ1351.7	4.00	14.8±0.4	6.9±0.9	960803_062202	A/2	30×300	300
S I λ1295.7	4.05	16.1±1.2	8.4±2.3	960804_050214	A/4	10×120	120
S I λ1300.9	4.05	15.3±0.6	6.8±1.3	960804_050214	A/4	10×120	120
C I λ1244.5	4.16	16.7±1.5	8.5±3.0	960803_025118	A/2	30×300	300
C I λ1249.4	4.16	17.1±1.6	9.3±2.9	960803_025118	A/2	30×300	300
C I λ1252.2	4.16	16.5±1.0	8.2±2.0	960803_025118	A/2	30×300	300
C I λ1315.9	4.14	14.7±0.8	5.8±2.0	960805_060417	A/2	10×200	400
C I λ1354.3	4.14	15.9±0.9	9.0±1.6	960803_062202	A/2	30×300	300
N I λ1319.7	4.21	15.7±0.5	8.1±1.0	960805_060417	A/2	10×200	400
O I λ1355.6	4.18	15.4±0.9	8.2±1.7	960803_062202	A/2	30×300	300
O I λ1355.6	4.18	15.3±0.5	8.0±1.0	960805_010431	A/2	10×300	400

[a]The notations conventionally used in SUMER file names were used to specify the observing times. For example, 960805_021923 represents 02h 19m 23s UT on 5 August 1996.

Table 2: Width measurements of EUV and FUV lines emitted by neutrals and singly ionized atoms.

Line	log T (K)	v_{meas} (km s^{-1})	v_{solar} (km s^{-1})	Obs Time[a]	Det/Slit	FOV ($''$)	Exp (s)
S I λ1412.9	4.05	15.6±1.2	9.4±2.0	960805_021923	A/2	10×200	400
N I λ1134.4	4.22	21.8±1.2	14.9±1.8	960805_033419	A/2	10×200	400
N I λ1135.0	4.22	21.7±1.2	14.7±1.8	960805_033419	A/2	10×200	400
O I λ925.0	4.23	24.0±2.2	13.5±3.9	960805_103024	A/4	100×100	110
O I λ929.5	4.23	25.0±2.0	15.3±3.3	960805_103024	A/4	100×100	110
O I λ935.2	4.23	25.4±1.9	16.1±3.0	960805_103024	A/4	100×100	110
O I λ1152.2	4.21	22.2±1.2	14.6±1.8	960723_100248	A/4	100×120	50
O I λ1040.9	4.21	22.5±1.2	14.1±1.9	960803_000445	A/2	27×250	300
O I λ1041.7	4.21	21.1±1.4	11.8±2.5	960803_000445	A/2	27×250	300
N II λ645.0	4.35	21.9±0.9	16.2±1.2	960722_181539	A/4	10×120	120
Fe II λ1361.4	4.26	20.0±0.9	15.2±1.2	960803_062202	A/2	30×300	300
S II λ1253.8	4.36	20.7±1.8	15.0±2.5	960803_025118	A/2	30×300	300
Si II λ1533.4	4.36	22.3±2.0	18.6±2.4	960712_051215	A/2	29×200	350
C II λ1036.3	4.57	27.7±2.4	21.4±3.1	960803_004947	A/2	30×300	300

[a]The notations conventionally used in SUMER file names were used to specify the observing times. For example, 960805_021923 represents 02h 19m 23s UT on 5 August 1996.

Table 3: Line optical depths inferred from the line ratios at disk center.

Line 1 / Line 2	Ratio ($\tau_0 = 0$)	Observed Ratio	τ_0 (Line 1)
O I $\lambda\lambda$1355.6/1358.5	3.27[a]	2.94±0.13	0.5
O I $\lambda\lambda$1040.9/1041.7	3.00	1.14±0.07	80
C II $\lambda\lambda$1037.0/1036.3	2.00	1.25±0.06	6.0
S II $\lambda\lambda$1253.8/1250.5	2.00	2.02±0.12	0.0
Si IV $\lambda\lambda$1393.8/1402.8	2.00	2.00±0.30	0.0
C IV $\lambda\lambda$1548.2/1550.8	2.00	2.12±0.24	0.0
N V $\lambda\lambda$1238.8/1242.8	2.00	2.10±0.24	0.0
S VI $\lambda\lambda$933.4/944.5	2.00	2.05±0.12	0.0
O VI $\lambda\lambda$1031.9/1037.6	2.00	2.02±0.17	0.0
Ne VIII $\lambda\lambda$770.4/780.3	2.00	1.91±0.15	0.3
Mg X $\lambda\lambda$609.8/625.0	2.00	2.12±0.24	0.0

[a]From the data given by Carlsson & Judge (1993)

Table 4: Non-thermal motions in quiet Sun regions on the disk.

Line	T (K)	ξ (km s^{-1})	σ_ξ (km s^{-1})	log I-ξ Correlation
C I λ1315.9	1.38×10^4	3.7		
N I λ1319.7	1.62×10^4	6.7		
O I λ1355.6	1.51×10^4	7.0	1.5	0.11
S II λ1253.8	2.29×10^4	14.6	2.4	0.50
C II λ1036.3	3.72×10^4	15.9	3.4	0.57
C II λ1037.0	3.72×10^4	16.5		
Si IV λ1393.8	7.08×10^4	22.6		
Si IV λ1402.8	7.08×10^4	23.2	4.5	0.64
C IV λ1548.2	1.00×10^5	25.0	4.0	0.61
C IV λ1550.8	1.00×10^5	25.1		
N V λ1238.8	1.74×10^5	27.6	4.2	0.43
N V λ1242.8	1.74×10^5	26.1		
S VI λ933.4	1.74×10^5	28.2	4.3	0.35
O VI λ1037.6	2.75×10^5	29.0	4.6	0.30
Ne VIII λ770.4	5.75×10^5	24.6	2.5	0.29
Mg X λ625.0	1.02×10^6	23.2	5.2	0.13
Fe XII λ1242.0	1.41×10^6	16.4	7.0	

Table 5: Dependence of the measured non-thermal motions on the exposure time.

Line	ξ (km s^{-1})	Obs Time[a]	FOV ($''$)	Exp(s)
C II λ1036.3	16.6	960803_000445	27×250	300
	16.2	960805_200152	100×80	20
O VI λ1037.6	31.3	960803_000445	27×250	300
	27.1	960805_200152	100×80	20

[a]The notations conventionally used in SUMER file names were used to specify the observing times. For example, 960805_021923 represents 02h 19m 23s UT on 5 August 1996.

Table 6: Non-thermal velocities measured near limb.

Line	ξ (km s^{-1})	r/R	Obs Time[a]	FOV($''$)
O I λ1355.6	7.1	0.99	960804_005135	6×100
Si II λ1253.8	16.1	0.85	960812_163643	30×90
Si IV λ1393.8	24.9	0.96	960719_025402	30×120
Si IV λ1402.8	24.5	0.96	960719_025402	30×120
C IV λ1548.2	28.3	0.97	960712_221207	25×120
C IV λ1550.8	28.4	0.97	960712_221207	25×120
N V λ1238.8	29.5	0.85	960812_163643	30×90
N V λ1242.8	26.4	0.85	960812_163643	30×90
Ne VIII λ770.4	28.1	0.97	960712_221207	25×120
Mg X λ625.0	22.3	0.85	960812_163643	30×90

[a]The notations conventionally used in SUMER file names were used to specify the observing times. For example, 960805_021923 represents 02h 19m 23s UT on 5 August 1996.